The variation and visualisation of elastic anisotropy in rock forming minerals

David Healy[1], Nicholas E. Timms[2] & Mark A. Pearce[3]

[1]: School of Geosciences, King's College, University of Aberdeen, Aberdeen AB24 3UE, United Kingdom

[2]: Space Science and Technology Centre, School of Earth and Planetary Sciences, Curtin University, Perth, GPO Box U1987, WA 6845, Australia

[3]: CSIRO Mineral Resources, Australian Resources Research Centre, 26 Dick Perry Avenue, Kensington, WA 6151, Australia

*corresponding author: d.healy@abdn.ac.uk

Abstract

All minerals behave elastically, a rheological property that controls their ability to support stress, strain and pressure, the nature of acoustic wave propagation and influences subsequent plastic (i.e. permanent, non-reversible) deformation. All minerals are intrinsically anisotropic in their elastic properties – that is, they have directional variations that are related to the configuration of the crystal lattice. This means that the commonly used mechanical elastic properties that relate elastic stress to elastic strain, including Young's modulus (E), Poisson's ratio (ν), shear modulus (G) and linear compressibility (β), are dependent on crystallographic direction. In this paper, we explore the ranges of anisotropy of E, ν, G and β in 86 rock-forming minerals, using previously published data, and show that the range is much wider than commonly assumed. We also explore how these variations (the directionality and the magnitude) are important for fundamental processes in the solid earth, including deformation (mechanical) twinning, coherent phase transformations and brittle failure. We present a new open source software package (AnisoVis, written in MATLAB), which we use to calculate and visualise directional variations in elastic properties of rock-forming minerals. Following previous work in the fields of chemistry and materials, we demonstrate that by visualising the variations in elasticity, we discover previously unreported properties of rock forming minerals. For example, we show previously unreported directions of negative Poisson's ratio and negative linear compressibility and we show that the existence of these features is more widespread (i.e. present in many more minerals) than previously thought. We illustrate the consequences of intrinsic elastic anisotropy for the elastic normal and shear strains within α-quartz single crystal under different applied stress fields; the role of elastic anisotropy on Dauphiné twinning and the α-β phase transformations in quartz; and stress distributions around voids of different shapes in talc, lizardite, albite, and sanidine. In addition to our specific examples, elastic anisotropy in rock-forming minerals to the degree that we describe has significant consequences for seismic (acoustic) anisotropy, the focal mechanisms of earthquakes in anisotropic source regions (e.g. subducting slabs), for a range of brittle and ductile deformation mechanisms in minerals, and geobarometry using mineral inclusions.

Introduction

The elastic deformation of rock-forming minerals plays an important role in many earth processes. The increased availability of measured or calculated elastic properties of whole rocks and of specific rock-forming minerals has led to advances in many fields of earth science, including seismology, geodynamics, tectonics and metamorphism. Minerals have long been known to display anisotropy – directional variations – in their elastic properties (Mandell, 1927; Birch & Dancroft, 1938; Hearmon, 1946), and that these variations show a close relationship to the symmetry of the mineral crystallographic structure. Advances in laboratory methods of measurement (acoustic velocities, Brillouin scattering, resonant ultrasound) and in theoretical techniques for *ab initio* calculations has allowed scientists to quantify this anisotropy for a wide range of rock forming minerals. For this paper we have collected 246 published datasets (measurements or *ab initio* calculations) of anisotropic elastic properties covering 86 distinct minerals. Elastic anisotropy is fully described by a fourth rank tensor (compliance or stiffness, see below), and published data are commonly presented in a Voigt matrix format, listing up to 21 independent values (depending on the crystal symmetry class), whereas elastically isotropic minerals require only 2 independent values. A key aim of this paper is to use published data to visualise and explore elastic anisotropy in rock forming minerals using familiar measures, such as Young's modulus and Poisson's ratio, but presented in novel formats and thereby render the increasing volume of data more transparent to analysis. As noted by previous authors (Karki & Chennamsetty, 2006; Lethbridge et al., 2010; Marmier et al., 2010; Gaillac et al., 2016), graphical depictions of the directional variation of elastic properties provide new opportunities to relate the quantitative data to the crystalline structure of the mineral. This in turn allows us to relate the observed or predicted mechanical and chemical behaviour of the mineral to specific crystallographic directions.

It has long been recognized that the velocity of seismic waves passing through rocks is a direct function of the minerals' elastic properties and their density, expressed through the Christoffel equation (Christoffel, 1877; Zhou & Greenhalgh, 2004). By considering rocks as polycrystalline aggregates various workers have modelled seismic velocities, and their anisotropy, by combining single mineral elasticity data with different averaging schemes due to Reuss, Voigt or Hill (e.g. Mainprice, 1990; Lloyd & Kendall, 2005). This 'rock recipe' approach has improved our understanding of the composition and structure of the lower crust and mantle and provided useful constraints for alternative models for observed variations in seismic anisotropy beneath continents and around arcs (e.g. Kern, 1982; Tatham et al., 2008; Healy et al., 2009).

Inclusions of one mineral or fluid within another host mineral have been used to estimate pressures at the time of inclusion or entrapment (Rosenfeld & Chase, 1961; Rosenfeld, 1969; Chopin, 1984; Gillet et al., 1984; van der Molen & van Roermund, 1986; Angel et al., 2014; Angel et al., 2015). The analysis critically depends on the elastic properties of the host mineral and, in the case of solid inclusions, of the inclusion itself, typically expressed as the bulk and shear moduli (e.g. Mazzucchelli et al., 2018). The underlying theory is based on the classical analysis by Eshelby (1957, 1959) who derived the equations for the deformation within an ellipsoidal inclusion and host due to the imposition of a far-field load. Most of the work to date has simplified the analysis to assume isotropy in both the inclusion and the host, although see Zhang (1998) for a rare exception. Therefore, the full effects of host minerals and inclusion elastic anisotropy on inclusion-based geobarometry have not yet been rigorously investigated. Furthermore, fluid inclusions can decrepitate – i.e. fracture their host and dissipate their fluid – if their internal overpressure rises to a

critical value that exceeds the local strength of the enclosing grain. The basis for predicting this behaviour is linear elastic fracture mechanics (LEFM), and the assumption of elastic isotropy is nearly ubiquitous (e.g. Lacazette, 1990).

Permanent, non-reversible (i.e. plastic) deformation of minerals is invariably preceded by an elastic response prior to some form of yield condition being reached. For example, the elastic properties of minerals are important in the analysis of brittle cracking at the grain scale. As noted above for the decrepitation of fluid inclusions, the dominant paradigm for this analysis is linear elastic fracture mechanics (LEFM), and the assumption of elastic isotropy. This is important because faults and fractures in rocks are composite structures, built by the interaction and coalescence of many smaller cracks that nucleate at the scale of individual grains i.e. within elastically anisotropic crystals. Jaeger & Cook (1969) used the equations published by Green & Taylor (1939) to consider the stresses developed at the edges of circular holes in anisotropic rocks. In their analysis (repeated in Pollard & Fletcher, 2005), they dismissed the significance of elastic anisotropy because the ratio of maximum to minimum Young's modulus in rocks is 'rarely as high as 2'. Timms et al. (2010) conducted novel indentation experiments in a single crystal of quartz and produced a type of cone fracture with variations in opening angle and crack length that have a trigonal symmetry radiating from the point of contact, and thus demonstrated the key role played by the elastic anisotropy in controlling the fracture geometry. In the same study, these authors confirmed that elastic anisotropy plays a significant role in controlling the focal mechanisms (moment tensors) of acoustic emission events at the scale of a single crystal.

Poisson's ratio appears as a term in, for example, the equations describing fracture toughness and indentation, and therefore the precise value of Poisson's ratio is important. Poisson's ratio for isotropic materials is constrained to lie between 0.5 and −1, but there are no theoretical limits for anisotropic materials (Ting & Chen, 2005). Materials with Poisson's ratio less than 0 are termed 'auxetic' (Lakes, 1987; Baughman et al., 1998a; Prawoto, 2012; Pasternak & Dyskin, 2012). Fracture toughness and resistance to indentation increase as Poisson's ratio approaches the lower (isotropic) limit of −1.0 (Yeganeh-Haeri et al., 1992). In rock forming minerals, negative Poisson's ratios have already been documented for α-cristobalite (Yeganeh-Haeri et al., 1992), for quartz at the α-β phase transition (Mainprice & Casey, 1990), for talc (Mainprice et al., 2008), and for calcite and aragonite (Aouni & Wheeler, 2008). A key question therefore is to determine if there are other rock forming minerals with the same properties, and for which specific crystallographic directions. In a recent review of data on Poisson's ratio in engineering materials, Greaves et al. (2011) pointed out that the brittle-ductile transition at the grain scale is also a function of the elastic properties and therefore likely dependent on direction in strongly anisotropic materials.

Elastic properties, and anisotropy, is also known to influence the 'ductile' or plastic deformation of minerals, and has a role in twinning, crystal plasticity (dislocation creep) and phase transformations (e.g. Tullis, 1969; Christian & Mahajan, 1995; Timms et al., 2018). The role of mineral elasticity is also important for inhomogeneous distribution of stresses at the grain scale necessary for driving pressure solution creep, and is either treated implicitly (e.g., Wheeler, 1992) or explicitly (e.g., Wheeler, 2018). However, in many studies of rock deformation, minerals are commonly assumed to be elastically isotropic and scalar mean values of elastic moduli are used, and/or elastic strains are assumed to be small relative to plastic deformation and so ignored (e.g., in visco-plastic self-consistent (VPSC) code) (Tomé & Lebensohn, 2014).

Given the key role that the elastic behavior of minerals plays in so many fundamental geological processes, the scientific need to explore, understand and quantify directional variations in elastic properties in minerals is clear, as is the need to develop better approaches to their graphical visualisation. It is very difficult to full appreciate the variations in elastic properties of a mineral simply by inspection of the 4th rank stiffness (or compliance) tensor, even in reduced form (Voigt notation; see below). A related requirement is the ability to investigate the interactions of mineral elastic anisotropy with imposed pressure, stress, or strain. However, the visualisation and full appreciation of the properties of 2nd rank tensors, such as stress and strain, also presents challenges. No single surface can simultaneously portray the full anisotropy quantified by the diagonal (normal) and off-diagonal (shear) components of these tensorial mechanical quantities. Depictions of strain (or stress) as ellipsoids using only the principal values as semi-axes fail to quantify the directional variations in shear strain (or stress) and cannot easily show examples with mixed positive and negative principal values. We believe there are clear educational benefits to alternative approaches to visualising stress and strain, which students commonly find challenging, both conceptually and from a 3-dimensional cognition perspective. For example, most geological textbooks either illustrate stress or strain as ellipses/ellipsoids of the normal component only (with the limitations described above), Mohr diagrams, or written out in matrix notation. Furthermore, a common misnomer that some minerals are isotropic in material properties undoubtedly stems from the strong emphasis on optical properties of minerals in most undergraduate mineralogy courses. Software tools with the capability of comparative visualisation of various physical properties of minerals in 2- and 3-dimensions, including elastic, optical, and acoustic anisotropy have a valuable place in teaching and learning in mineralogy and in scientific research.

While the number of published datasets for single mineral elastic anisotropy continues to increase, there are relatively few publications that have reviewed or synthesised the available data. Gercek (2007) provided a useful review of Poisson's ratio for rocks and included some data for specific minerals. A more recent review of Poisson's ratio in rocks (Ji et al., 2018) also contained data for minerals, but used their calculated Voigt-Reuss-Hill average values rather than quantify their anisotropy. Workers in the fields of chemistry, physics and engineering have published methods and tools for visualising the elastic anisotropy of various groups of solid elements and compounds (Karki & Chennamsetty, 2006; Lethbridge et al., 2010; Marmier et al., 2010; Gaillac et al., 2016), and these predominantly focus on Poisson's ratio. In earth sciences, the MTEX toolbox for the analysis and modelling of crystallographic textures from electron backscatter diffraction (EBSD) data provides stereographic projections of elastic properties, such as Young's modulus, for single minerals (Hielscher, R. & Schaeben, H., 2008; Mainprice et al., 2011). The MSAT toolbox for seismic anisotropy also contains options for plotting the elastic anisotropy of rocks and minerals (Walker & Wookey, 2012). Both MTEX and MSAT provide one or more options for displaying the elastic properties of minerals, but their main focus is on the analysis of textures and seismic (acoustic) velocity anisotropy, respectively.

In this paper we present the AnisoVis toolbox, a collection of new MATLAB scripts based on published methods with a graphical user interface (GUI), to explore the range of elastic anisotropy displayed by rock forming minerals. Specifically, AnisoVis depicts the magnitude of the directional variations in elastic properties such as Young's modulus (E), Poisson's ratio (ν), shear modulus (G) and linear compressibility (β) using a range of 2- and 3-dimensional representations of each elastic property to enable a complete assessment of the anisotropy in relation to the crystal

symmetry. We exploit the large database of published elastic constants for rock-forming minerals to systematically assess the anisotropy of different elastic properties as a function of temperature and pressure (where possible), giving new insights into the elastic behaviour of rock-forming minerals. Most of the figures presented in this paper have been produced from the AnisoVis toolbox, which is freely available on the web.

A table of symbols and terms used in this paper is provided in Table 1. We follow the geological convention that compressive stress is positive, tensile stress is negative. Elastic properties are reported in SI units. In Section 2 we review the theoretical basis of linear elasticity and the formal description of elastic anisotropy in terms of the key equations. We then describe the methods we use to visualise and quantify the directional variations in elastic properties for any given mineral. We present two sets of results. Firstly, we analyse general trends in the database of 86 distinct minerals with 246 separate elasticity datasets from published sources, and summarise the degree of anisotropy to be found in rock forming minerals. Secondly, we analyse specific examples and focus on their response to applied deformation. We review the key issues raised by these analyses in the Summary. The Appendix contains benchmarks of the calculations performed in AnisoVis in comparison to published output from previous workers.

Quantity	**Symbol**	**Default SI unit**
Young's modulus	E	Pa
Poisson's ratio	ν	
Shear modulus	G	Pa
Linear compressibility	β	Pa^{-1}
Bulk modulus	K	Pa
Compliance	s	Pa^{-1}
Stiffness	c	Pa
Stress	σ	Pa
Strain	ε	
Normal stress	σ_n	Pa
Shear stress	τ	Pa
Normal strain	ε_n	
Shear strain	γ	
Unit vectors parallel to crystallographic axes	***a, b, c***	Miller notation

Table 1. List of symbols and terms used in this paper, together with their default units (if any).

2. Theory and underlying equations

The elastic anisotropy of a solid material is described by a fourth rank tensor, either the compliance s_{ijkl} or its inverse, the stiffness c_{ijkl}. For linear elastic deformation, the generalised form of Hooke's Law can be written as:

$$\varepsilon_{ij} = s_{ijkl}\, \sigma_{kl} \qquad (1)$$

where ε_{ij} and σ_{ij} are the second rank tensors of strain and stress, respectively. Alternatively, equation (1) can be written as:

$$\sigma_{ij} = c_{ijkl}\, \varepsilon_{kl} \qquad (2).$$

Symmetry considerations lead to $s_{ijkl} = s_{ijlk}$ and $s_{ijkl} = s_{jikl}$ (Nye, 1985). The corollary of these relationships is that the number of independent (potentially unique) components of s_{ijkl} is reduced from 81 ($=3^4$) to 36. The same applies to c_{ijkl}. The elastic compliance s or stiffness c of a crystal can therefore be represented in a more compact form, known as the Voigt matrix. This is a square 6 x 6 matrix where, for example, the elements of elastic stiffness are defined as $c_{IJ} = c_{ijkl}$, where $I = ij$ and $J = kl$. There are six different permutations of $I(J) = ij(kl)$, the details of which are listed in Nye (1985) and more recently in Almqvist & Mainprice (2017).

The measured and calculated elastic properties of single crystals are reported in Voigt matrix notation (s_{IJ}, c_{IJ}), where the indices I, J (=1,2,3) relate to a standard Cartesian reference frame (x=1, y=2, z=3). The relationship between any specific crystal lattice and this Cartesian reference is arbitrary, but we adopt the convention described in Britton et al. (2016). In this system:

- the unit cell lattice vectors ***a***, ***b***, and ***c*** form a right-handed set,
- ***c*** is parallel to Cartesian z,
- ***b*** lies in the Cartesian y-z plane at angle α to ***c***, and
- ***a*** is directed at angle β to ***c*** and γ to ***b***.

Note that α is the angle between ***b*** and ***c***, β is the angle between ***c*** and ***a*** and γ is the angle between ***a*** and ***b*** (see Figure 1a).

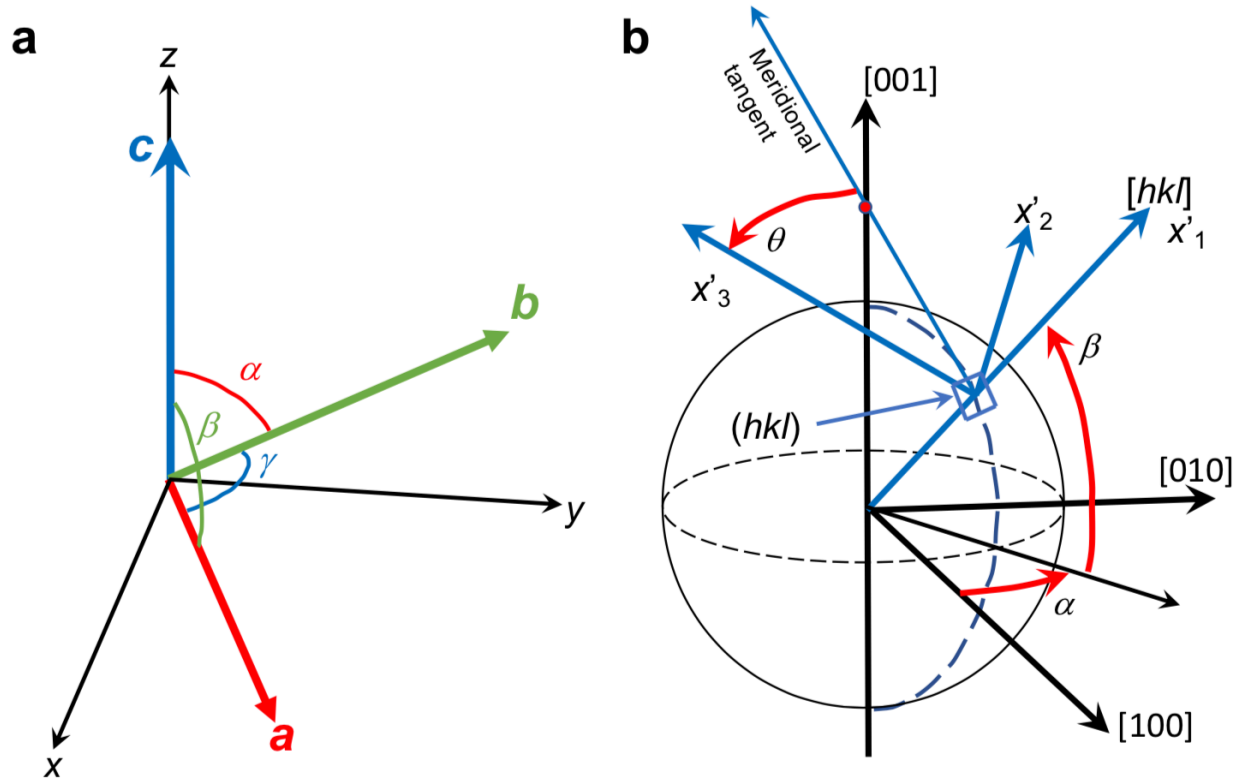

Figure 1. a) Crystallographic orientation convention (after Britton et al., 2016) and **b**) geometrical reference frame (after Turley & Sines, 1971) used in this paper.

Familiar elastic properties, such as Young's modulus (E), Poisson's ratio (ν) and shear modulus (G), can be expressed directly in terms of the components of the compliance matrix. For example, the Young's modulus of a single crystal for a uniaxial stress applied in the x-direction is:

$$E_x = E_1 = 1 / s_{11} \qquad (3)$$

and the Poisson's ratio for a uniaxial stress and axial strain along x and a lateral strain along y is

$$\nu_{xy} = -s_{21} / s_{11} \qquad (4)$$

Note that, in general for anisotropic materials, $\nu_{xy} \neq \nu_{yx}$ etc.

Guo & Wheeler (2006) note that although Poisson's ratio may be negative for some directions, these are often compensated by higher positive values in transverse directions perpendicular the minima in the same plane. They suggest a more useful measure of extreme auxeticity, the **areal Poisson's ratio**, defined as the average of all values of Poisson's ratio taken within the plane normal to a chosen direction. If the areal Poisson's ratio is negative this implies that a cylinder of the mineral would contract under a uniaxial compression, around the whole circumference, and not just along certain directions.

In order to calculate specific values of these elastic properties in more general directions within a crystal – i.e. not just along the axes of the default Cartesian reference frame – we need to transform the compliance matrix into a different reference frame. We follow the notation used by Turley & Sines (1971) based on Eulerian angles α, β and θ (see Figure 1b) that define the new Cartesian axes

(1', 2', 3' or x', y', z') in relation to the initial reference frame (1,2,3 or x, y, z). The transformation of compliance matrix s_{ijkl} to s'_{ijkl} is given by (Nye, 1985):

$$s'_{ijkl} = a_{im}\, a_{jn}\, a_{ko}\, a_{ip}\, s_{mnop} \qquad (5)$$

where the elements of the rotation matrix $\boldsymbol{a}$ are given by:

$$a_{ij} = \begin{bmatrix} A & B & C \\ (D\sin\theta + E\cos\theta) & (F\sin\theta + G\cos\theta) & H\sin\theta \\ (D\cos\theta - E\sin\theta) & (F\cos\theta - G\sin\theta) & H\cos\theta \end{bmatrix} \qquad (6)$$

where $A = \cos\alpha\cos\beta$, $B = \sin\alpha\cos\beta$, $C = \sin\beta$, $D = -\cos\alpha\sin\beta$, $E = -\sin\alpha$, $F = -\sin\alpha\sin\beta$, $G = \cos\alpha$, $H = \cos\beta$ (Turley & Sines, 1971).

Using the transformed compliance matrix s'_{ijkl}, we can now calculate the elastic properties for any general direction within the crystal defined by a unit vector with angles α, β and θ, for example:

$$E'_1 = 1 / s'_{11} \qquad (7)$$

$$G'_{12} = 1 / s'_{66} \qquad (8)$$

$$\nu'_{12} = -s'_{21} / s'_{11} \qquad (9)$$

To calculate the variation in any elastic property over all possible directions in 3D, we simply need to vary α and β over a unit sphere (α: 0-360°, β: 0-180°) and vary θ over a unit circle (θ: 0-360°).

Isotropic approximations of anisotropic elastic properties

Two useful 'averaging' schemes that can be applied to the full set of anisotropic elastic properties of polycrystals are those due to Reuss and Voigt (see Hill, 1952). The bulk and shear moduli in the Voigt scheme are defined as:

$$K^V = [(c_{11} + c_{22} + c_{33}) + 2(c_{12} + c_{23} + c_{31})]/9 \qquad (10)$$

$$G^V = [(c_{11} + c_{22} + c_{33}) - (c_{12} + c_{23} + c_{31}) + 3(c_{44} + c_{55} + c_{66})]/15 \qquad (11)$$

and in the Reuss scheme as:

$$K^R = 1/[(s_{11} + s_{22} + s_{33}) + 2(s_{12} + s_{23} + s_{31})] \qquad (12)$$

$$G^R = 15/[4(s_{11} + s_{22} + s_{33}) - 4(s_{12} + s_{23} + s_{31}) + 3(s_{44} + s_{55} + s_{66})] \qquad (13)$$

The Voigt average of any property always exceeds the Reuss average and the 'true' value lies somewhere in between. The Voigt-Reuss-Hill (VRH) average of a property is defined as the arithmetic mean of the Voigt and Reuss estimates e.g. $G^{VRH} = (G^V + G^R)/2$. Note that, although only formally defined for polycrystals and based on averaging over many grains, the Voigt, Reuss and VRH estimates are in practice useful for single crystals: if we consider a polycrystal made of many grains all aligned perfectly parallel, then the elastic anisotropy of this polycrystal is identical to that of the single crystal.

To plot the variations of disparate elastic properties across minerals with widely different symmetries and anisotropies, we use the Universal Anisotropy Index (A^U), of Ranganathan & Ostoja-Starzewski (2008), defined as:

$$A^U = 5\,\frac{G^V}{G^R} + \frac{K^V}{K^R} - 6 \qquad (14)$$

where G^V and K^V are the Voigt average shear and bulk moduli, respectively; and G^R and K^R are the Reuss average shear and bulk moduli, respectively.

3. AnisoVis – program description and visualisation methods

The visualisations of elastic anisotropy presented in this paper have been prepared using AnisoVis, a set of custom scripts linked to a graphical user interface (GUI) and written in MATLAB™. This code is available as an open source project on GitHub (link) and through the MathWorks™ FileExchange server (link). Single mineral elasticity values are supplied as input data, together with lattice parameters defining the unit cell and symmetry. The code then calculates the directional variations in elastic properties and produces outputs of the kinds shown in Figures 4-7. AnisoVis can also calculate the acoustic velocities (phase and group) and their polarisations, and the optical birefringence from the refractive indices. Over 240 data files for 86 different minerals are included (from published sources), and a user guide is provided with the software.

Installation and input file format

AnisoVis is installed by copying all of the files from the GitHub or Mathworks FileExchange server into a folder on the user's computer. AnisoVis will run on any computer with MATLAB installed, including running Windows, Mac OS X or different versions of Linux. After starting MATLAB, the working folder or directory should be set to the folder containing all of the installed source code. The application is started by typing 'AnisoVis' in the Command window of the MATLAB session. There is only one window in AnisoVis (Figure 2). Click 'Browse…' to show the standard dialog to open an input file of mineral properties. These are stored in formatted tab-delimited ASCII text files with an extension of '.mdf2' ('mineral data file'). The user guide supplied with the software has examples for each different mineral symmetry class.

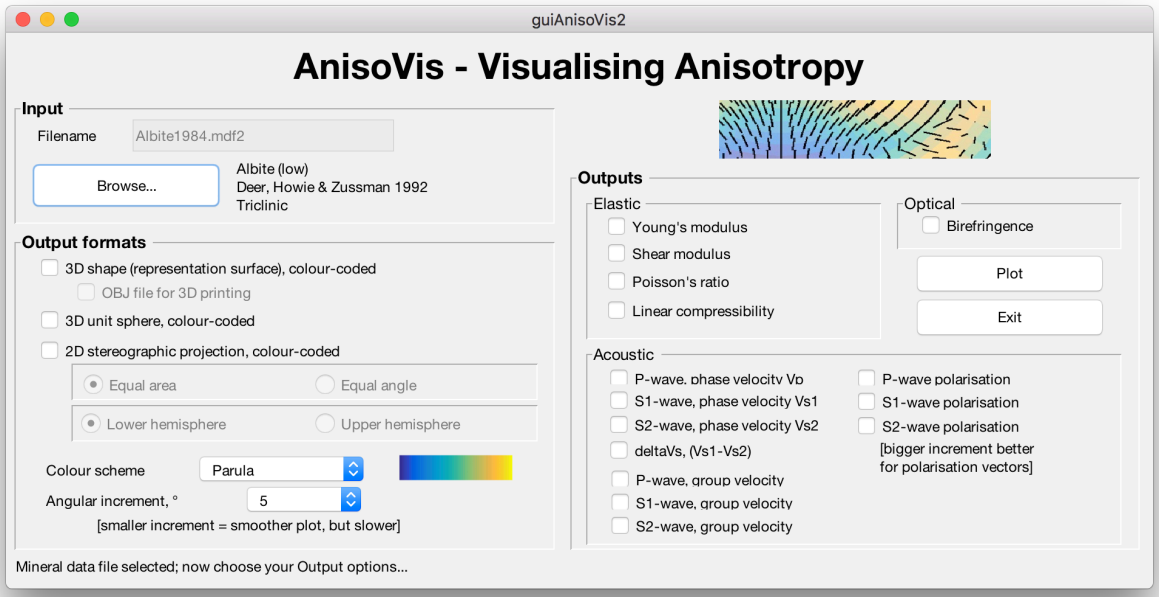

Figure 2. The graphical user interface in AnisoVis, showing the range of output options for elastic (and acoustic and optical) anisotropies.

Calculations

After selecting the required output formats (shape, sphere or stereogram) and anisotropic properties to be visualised (elastic, acoustic or optical), the user clicks Plot to generate the images. Calculations are performed using the equations for each property described above, looping through three-dimensional space with the specified angular increment. Smaller angular increments (e.g. 1-2°) take longer to run than larger increments (e.g. 5-10°). In the tests that we have conducted to date, run time has been very satisfactory, with most operations completed in a few seconds on standard desktop computers purchased within the last three years. The exception to this performance is when the angular increment is 1°, where run times are typically of the order of 1-2 minutes. We have implemented a MATLAB™ WaitBar to provide basic progress information for lengthier tasks.

Generating outputs

Output is directed to MATLAB figure windows, with one plotted property per figure window. These images are automatically saved as '.tif' files at 600 dpi resolution in the working folder. While each figure window is visible, the user can exploit standard MATLAB functionality to resize or reformat the figure as they wish, and can save the figure to a different filename or folder, or even a different graphic format (e.g. '.png' or '.jpeg'). The colour schemes used for the representation surfaces, unit spheres and stereograms can be varied using the drop-down list box in the main window. In addition to the standard MATLAB colour map of 'Parula' we offer 3 other choices from the cmocean colour map library (Thyng et al., 2016) using perceptually uniform scales ('Haline', 'Thermal' and 'Matter').

Visualising elastic anisotropy in 2-D and 3-D

As pointed out by Nye (1985), no *single* surface can represent the elastic behaviour of a crystal completely. However, we can plot specific surfaces that are useful in practice. To visualise the anisotropy of elastic properties of single crystals we use a mixture of 3D surfaces and 2D polar plots projected onto selected planes. We use representation surfaces (Nye, 1985) to generate 3D shapes where, for any given radius vector measured from the origin to the surface, the radius is proportional to the magnitude of the property in that direction. The magnitude of the property is also conveyed by a colour mapping applied to the surface. An alternative method is to plot the directional variation of a property projected onto a unit sphere, using a colour map to depict the magnitude. We can also use stereographic projections (lower hemisphere, equal area) to show directional variations in properties. Lastly, we can use polar plots to the variation of a property in selected crystallographic planes (e.g. [100], [010], [001]).

Challenges in visualising Poisson's ratio (ν) and shear modulus G

Any of the above methods of visualisation can be used for 'simple' elastic properties, such as Young's modulus or linear compressibility, where the property is a single scalar value for a given direction. Young's modulus is defined as the ratio of uniaxial stress to uniaxial strain and it is implicit that the directions of applied stress and measured strain are coincident (i.e. coaxial; Figure 3). However, for Poisson's ratio and shear modulus this is no longer the case. Poisson's ratio is defined as the ratio of (negative) lateral strain to the axial strain, and therefore involves two orthogonal directions (Figure 3). Shear modulus is defined as the ratio of the shear stress to the shear strain, again involving two orthogonal directions (see Figure 3). For a stress (normal or shear) applied in a specific direction, there is only one value of E, but there are many possible values of ν and G. It can be seen from Figure 3 that ν and G will vary according to the direction of the normal to the chosen direction [*hkl*], described by angle θ in the Turley & Sines (1971) notation. To plot representation surfaces for ν and G, we take their minimum and maximum values calculated over θ for an applied stress along each direction in 3D-space. In addition, as ν can be negative for some directions in some minerals, we further separate the minimum representation surfaces of Poisson's ratio into negative minimum and positive minimum components where appropriate.

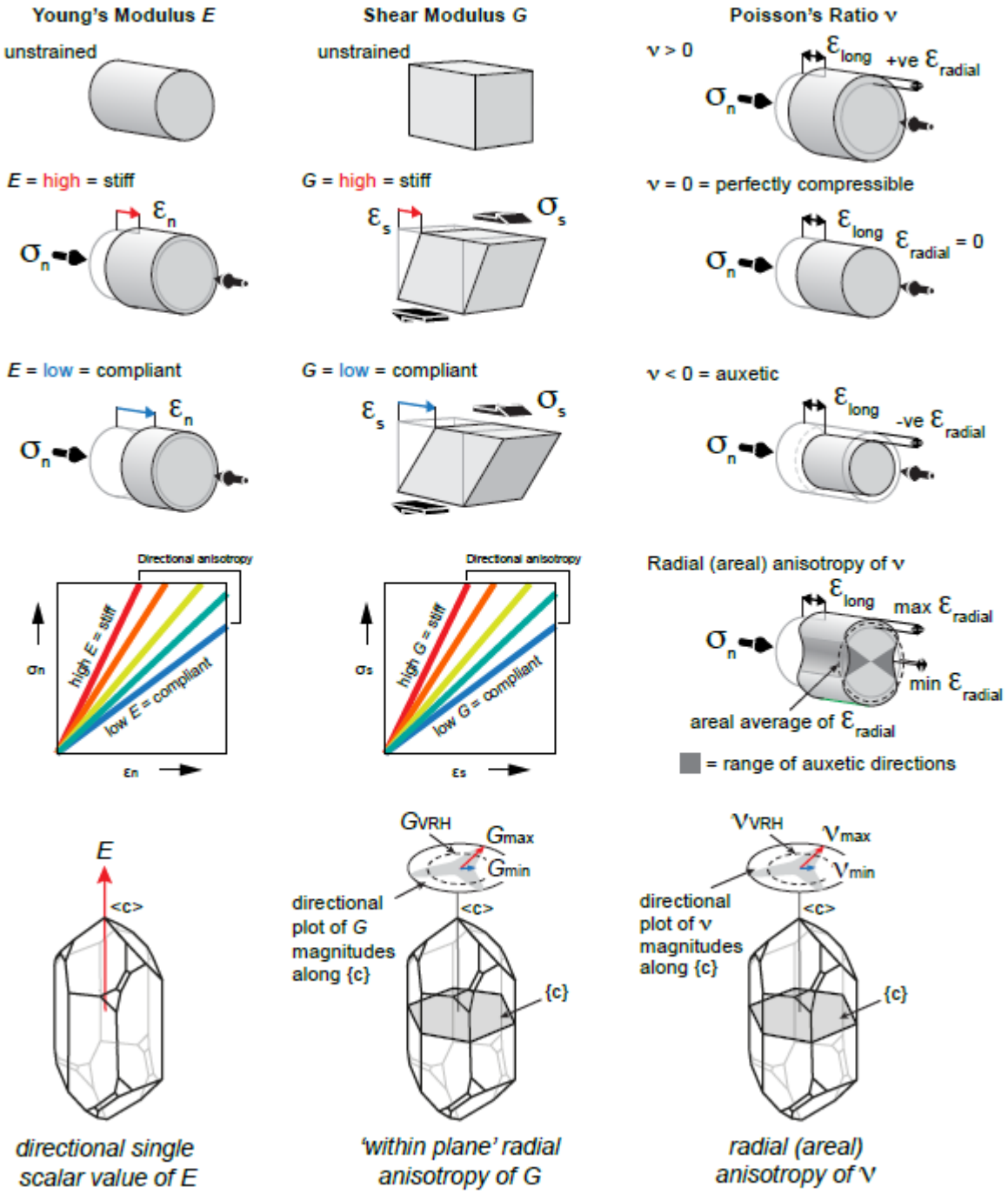

Figure 3. Schematic diagrams to illustrate the definitions of Young's modulus, Poisson's ratio, shear modulus in a 3D crystallographic reference frame, using α-quartz (trigonal) as an example.

Example: α-quartz (trigonal; Ogi et al., 2006)

To illustrate the different possibilities described above we use the elasticity of α-quartz as quantified by Ogi et al. (2006). The anisotropy of Young's modulus is shown in Figure 4 using a representation surface, a unit sphere, a stereogram and polar plots of E in the plane (100). The colour bar scale is the same in all plots for ease of comparison. Using AnisoVis, the user can rotate any of these plot views in the MATLAB figures to gain a better appreciation of the directional variations in relation to the crystallographic reference axes <a>, <b>, and <c>.

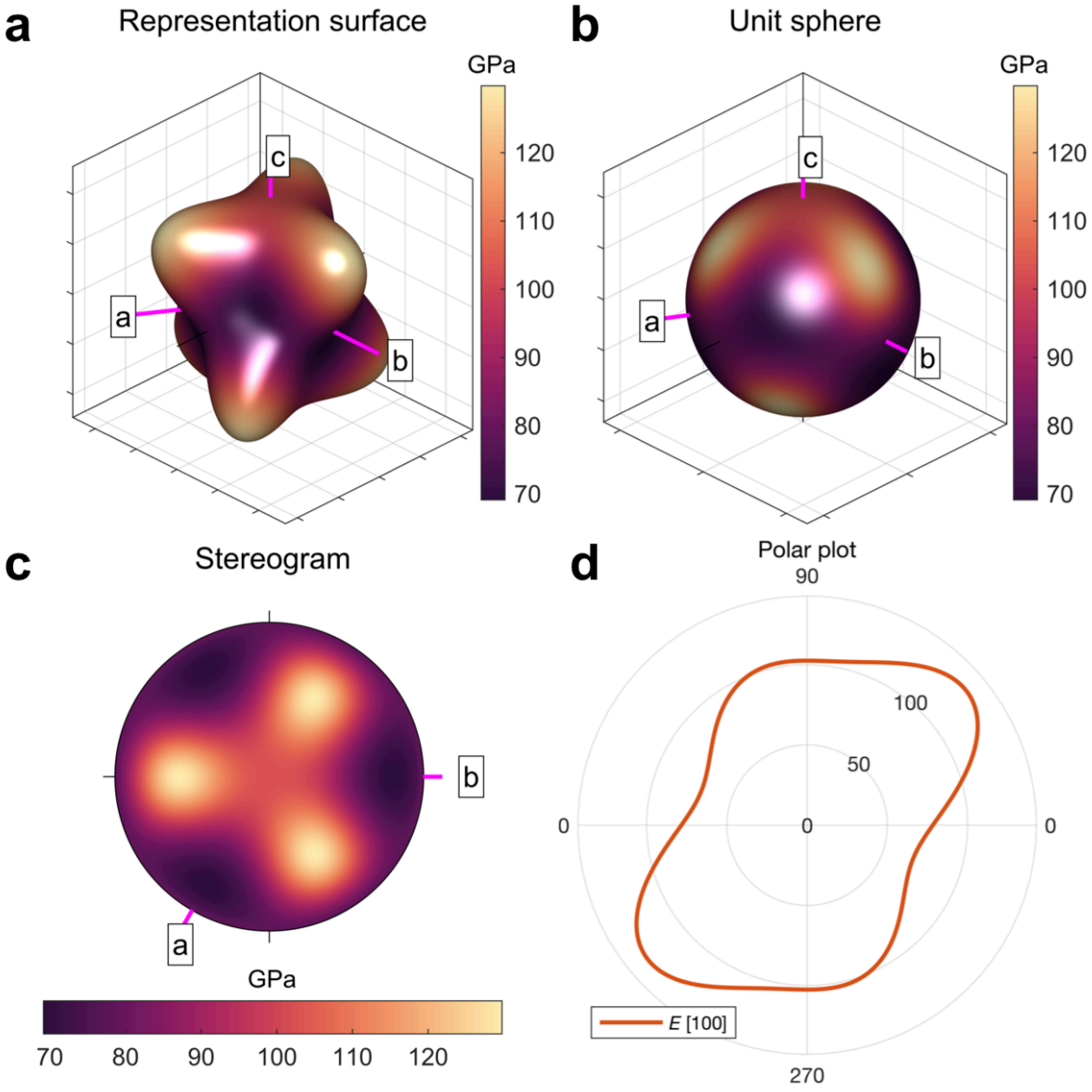

Figure 4. Alternative visualisations of the anisotropy of Young's modulus (E, in GPa) of α-quartz. **a**) 3D representation surface where the radius in any direction is proportional to the magnitude of E. **b**) Projection of E on to a unit sphere, colour coded by magnitude. **c**) Lower hemisphere, equal area stereographic projection. **d**) Polar plot of anisotropy of E in the [010] plane. Crystallographic axes <a>, <b>, and <c> shown in pink. VRH = Voigt-Reuss-Hill average value of E.

As noted above, the shear modulus is a function of shear stress in one direction and a shear strain in a perpendicular direction. Therefore, for any given crystallographic direction in 3D space [*hkl*] in an anisotropic crystal there are many possible values of G as the transverse component is rotated through the angle θ (see Figure 1b). In Figure 5 we show representation surfaces for the minimum and maximum values of G of α-quartz associated with each direction [*hkl*]. Polar plots are also shown for (010) and (001).

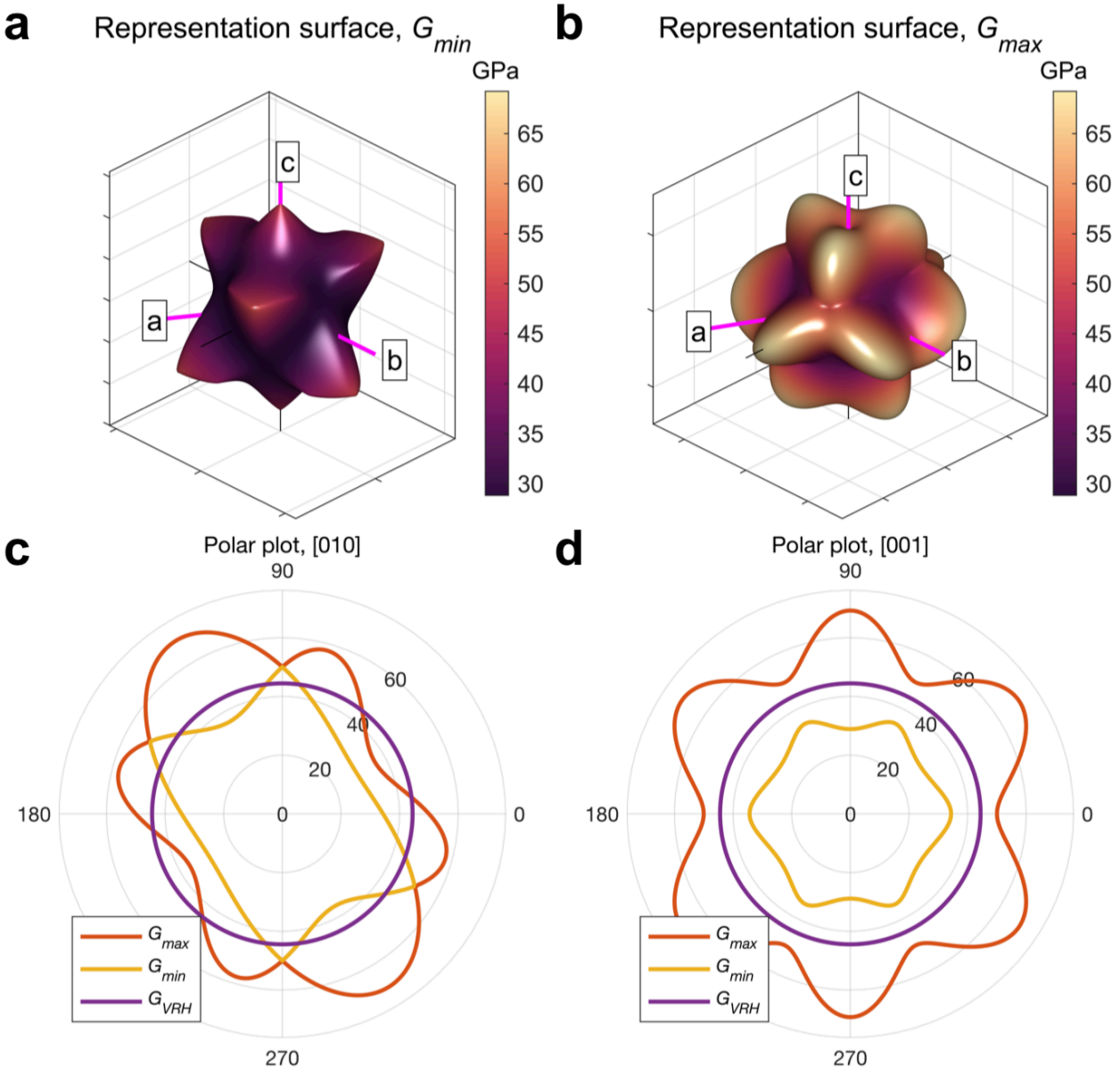

Figure 5. Alternative visualisations of the anisotropy of shear modulus (G, GPa) of α-quartz. **a-b**) 3D representation surfaces where the radius in any direction is proportional to the magnitude of G. Separate surfaces shown for minimum and maximum G. **c-d**) Polar plots of anisotropy of G in the [010] and [001] planes, respectively. Crystallographic axes <a>, <b>, and <c> shown in pink. VRH = Voigt-Reuss-Hill average value of G.

Visualising the directional variation of Poisson's ratio ν can pose further challenges. α-quartz is auxetic and has many directions that show negative Poisson's ratios. As for shear modulus, we show representation surfaces for both the minimum (Figure 6a-b) and maximum (Figure 6c) Poisson's ratios, but we separate the minimum Poisson's ratio plot into two surfaces: one for $\nu_{min} < 0$ (Figure 6a) and one for $\nu_{min} > 0$ (Figure 6b). We also include a plot for the areal Poisson's ratio – the value of Poisson's ratio averaged over all θ for each direction [hkl] (Figure 6d, after Guo & Wheeler, 2006). Polar plots for specific 2D planes can also be useful (Figure 6e-f).

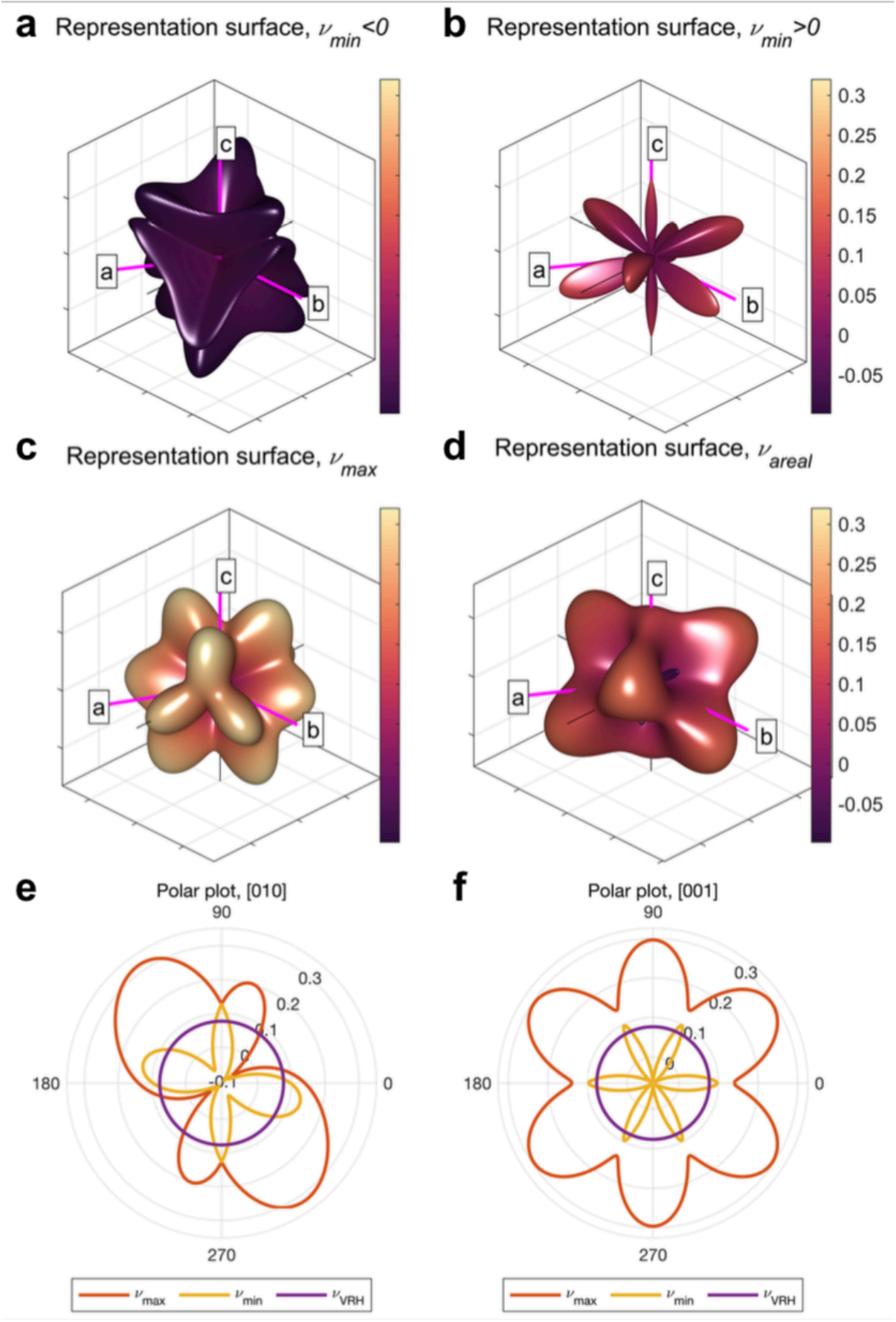

Figure 6. Alternative visualisations of the anisotropy of Poisson's ratio (ν) of α-quartz. **a**-d) 3D representation surfaces where the radius in any direction is proportional to the magnitude of ν. Separate surfaces shown for minimum negative, minimum positive, maximum and areal *n,* as

defined in the equations in Section N.N. **e-f**) Polar plots of anisotropy of ν in the [010] and [001] planes, with separate lines shown for ν_{min}, ν_{max} and ν_{VRH}. Crystallographic axes <a>, <b>, and <c> shown in pink. VRH = Voigt-Reuss-Hill average value of ν.

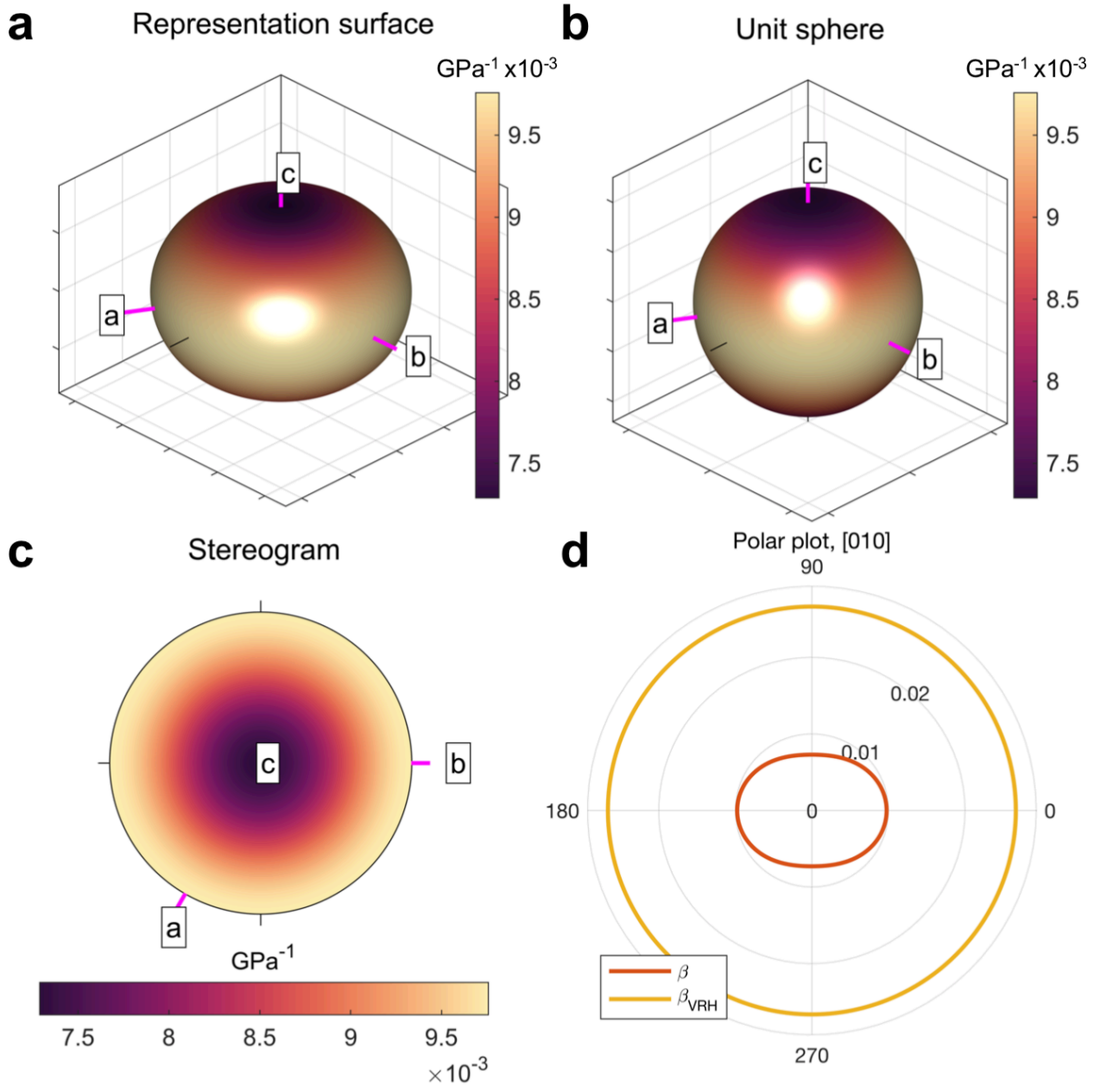

Figure 7. Alternative visualisations of the anisotropy of linear compressibility (β, in GPa^{-1}) of α-quartz. **a**) 3D representation surface where the radius in any direction is proportional to the magnitude of β. **b**) Projection of β on to a unit sphere, colour coded by magnitude. **c**) Lower hemisphere, equal area stereographic projection. **d**) Polar plot of anisotropy of β in the [010] plane. Crystallographic axes <a>, <b>, and <c> shown in pink. VRH = Voigt-Reuss-Hill average value of β.

The linear compressibility (β) of an anisotropic crystal quantifies the directional response to an applied hydrostatic load i.e. to pressure, not stress. For isotropic materials, the compressibility is a

scalar – directionally invariant – and is simply the inverse of the bulk modulus K ($\beta = 1 / K$). For anisotropic rock forming minerals, this is no longer the case and β varies with direction. Figure 7 shows the variation for α-quartz using the same types of plots as for Young's modulus (Figure 5). In summary, we note that as a corollary of the point made by Nye (1985) that no single surface can represent the full richness of the 4th rank elasticity tensor, neither can any one measure (e.g. E, G, ν or β) convey the complete behavior of an anisotropic mineral. The anisotropies of the different parameters (through these plots) should be used in combination to understand a specific problem.

Visualising second-rank tensors: stress and strain

To address the challenges in visualizing stress and strain described above, we use two separate graphical depictions, or glyphs, for the normal and shear components of the strain and stress tensors (Kratz et al., 2014). We use the Reynolds glyph for normal strains and stresses, as this can show positive and negative principal values (Moore et al., 1996). We use the HWY glyph to visualise the shear components of the strain and stress tensors (Hashash et al., 2003). Figures 8 and 9 show examples of the Reynolds and HWY glyphs for strains and stresses, respectively. Isotropic compaction plots as a single point in Mohr space (Figure 8a), and as a sphere using a Reynolds glyph (Figure 8b; shear strains are zero and so there is no HWY glyph). For a general triaxial strain with both shortening and stretching components, the Reynolds and HWY glyphs are shown in Figure 8d and 8e. Note that in the HWY glyph for shear strain the maxima are located at 45° to the principal axes, and the minima (0) are located along the principal axes. Triaxially compressive stress is shown in Figure 9a-c. Again, maxima of shear stress in the HWY glyph are at 45° to the directions of the principal (normal) stresses. For a general triaxial stress with components of compression and tension, the directional variations of normal and shear stress are shown in Figure 9d-f.

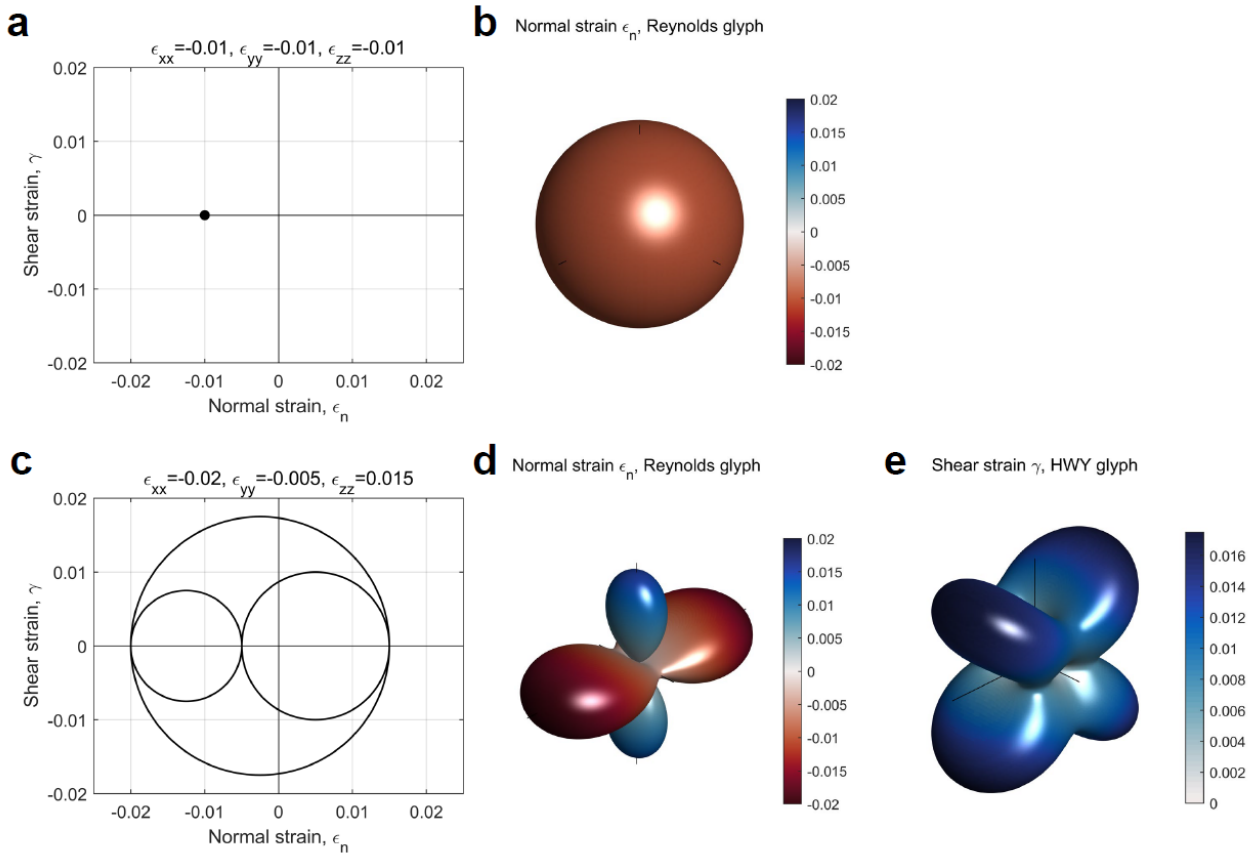

Figure 8. Examples of strain tensors depicted in Mohr space (ε_n, γ), and as Reynolds (normal strains, ε_n) and HWY (shear strains, γ) glyphs. **a**-**b**) Isotropic compaction (taken as negative, blue colour). **c**-**e**) Visualisations for a general triaxial strain. Note the lobes of extensional (blue) and contractional (red) strain in the normal strain plot (**d**).

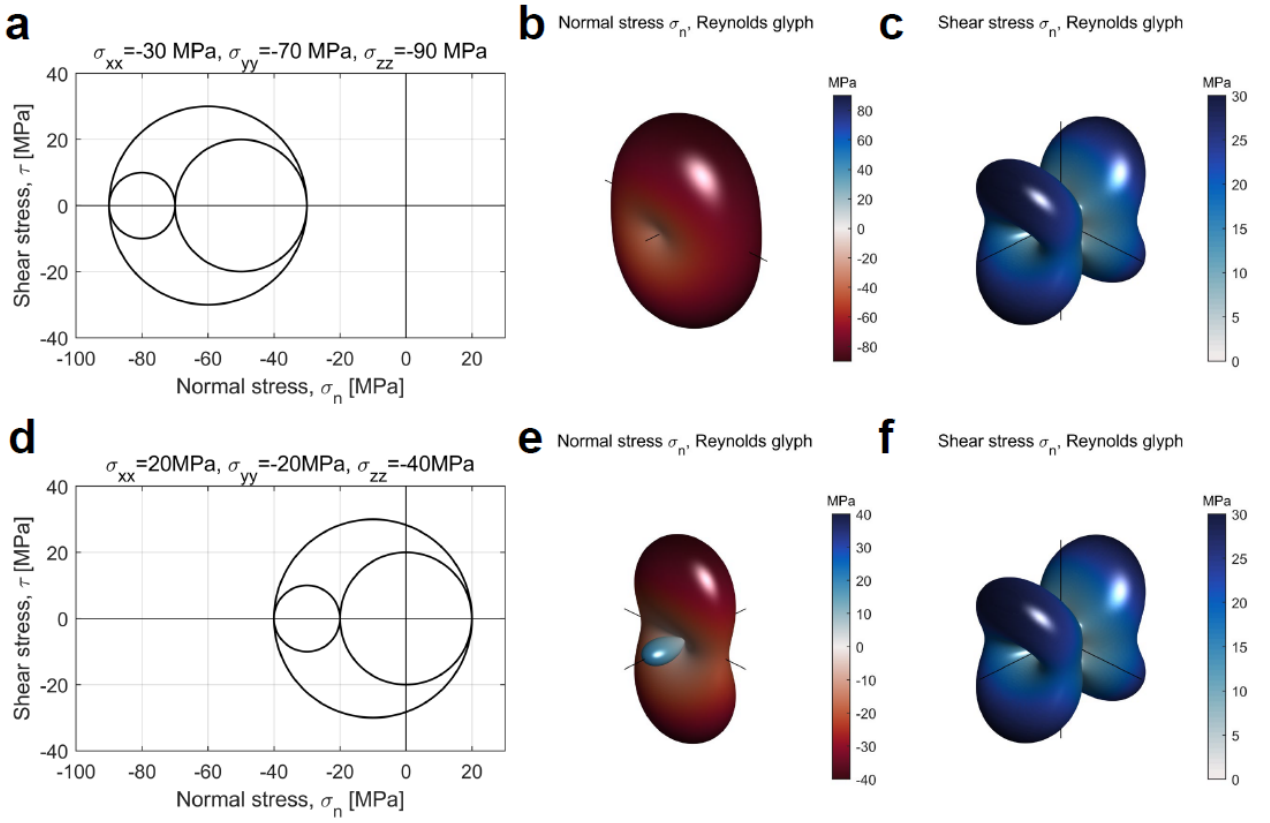

Figure 9. Examples of stress tensors depicted in Mohr space (σ_n, τ) and as Reynolds (normal stress, σ_n) and HWY (shear stress, τ) glyphs. **a-c**) Triaxial compression (taken as negative, blue colour). **d-f**) General triaxial stress with one principal stress tensile (σ_{xx}).

Data sources

The elastic properties of the minerals used in this study have been derived from previous compilations and original sources where possible. Many compilations of elastic and other physical properties are now available: see Bass (1995) and Almqvist & Mainprice (2017), and references therein. Note that most elastic properties are measured by laboratory methods whereas a minority are calculated from theory (*ab initio*). Single mineral lattice parameters have been extracted from the same publication as the elasticity data where possible, but if this was not available, we took representative values from Deer, Howie & Zussman (1992).

4. Results – General trends

From our database of published elastic properties of rock-forming minerals (246 data files covering 86 distinct minerals, all included with AnisoVis), we have calculated the maxima and minima for Young's modulus, Poisson's ratio, shear modulus and linear compressibility. In Figure 10 we show the variation in the anisotropy of Young's modulus (E) for 246 rock forming minerals as a function of A^U. If we consider a simple measure of the anisotropy of E as the ratio between the maximum and minimum values, it is clear that most minerals display significant anisotropy with E_{max}/E_{min} often greater than 2. With increasing A^U, many minerals show E_{max}/E_{min} ratios of about 4. Figure 11 shows the anisotropy of shear modulus (G) for the same rock forming minerals, plotted against

A^U. The anisotropy of G, simply defined as G_{max}/G_{min}, is less than that shown for E, and there is a general pattern of decreasing anisotropy of G with increasing A^U.

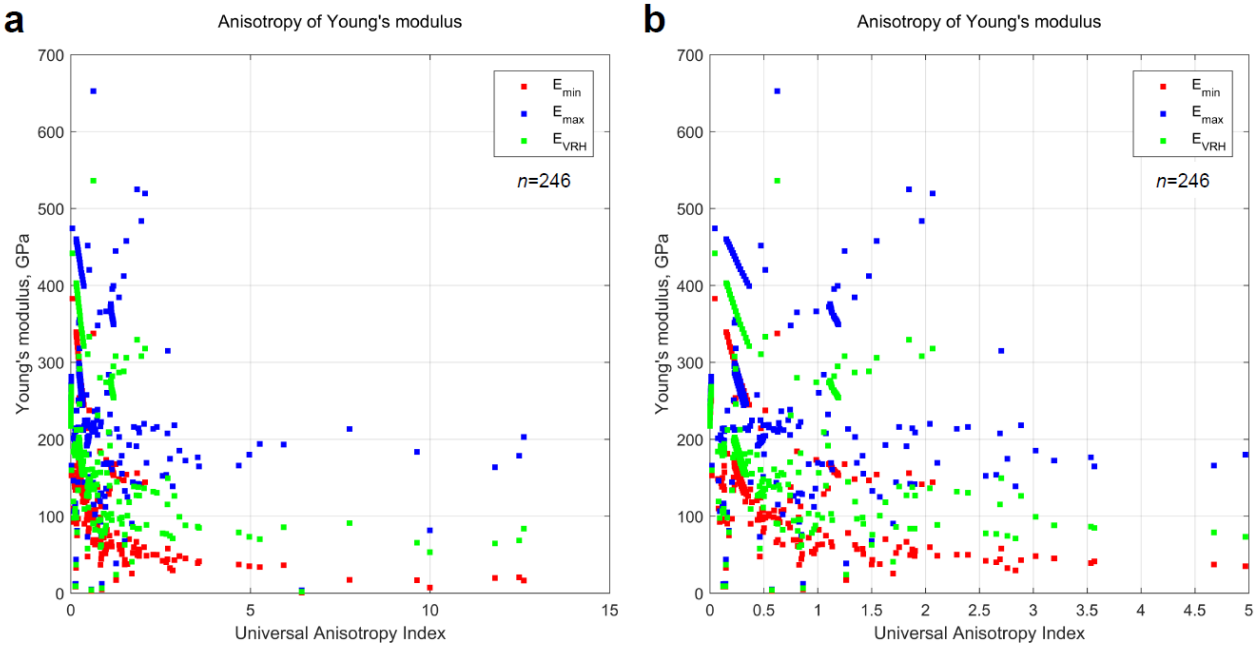

Figure 10. Anisotropy of Young's modulus in rock-forming minerals (n=246) plotted against the Universal Anisotropy Index (A^U) of Ranganathan & Ostoja-Starzewski (2008). E_{VRH} is the Voigt-Reuss-Hill average of E. Many minerals display anisotropy of E (E_{max}/E_{min}) of 2 or more. **b**) Close-up of data in **a**) for UAI up to 5.

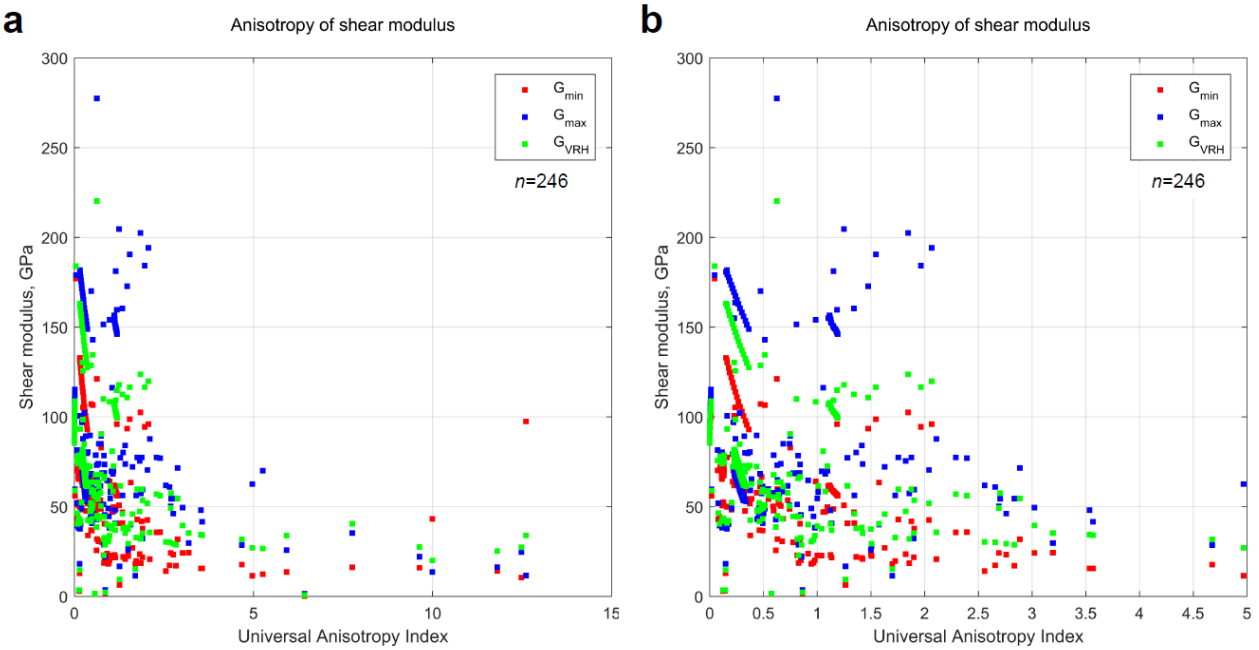

Figure 11. Anisotropy of shear modulus in rock-forming minerals (n=246) plotted against the Universal Anisotropy Index of Ranganathan & Ostoja-Starzewski (2008). G_{VRH} is the Voigt-Reuss-Hill average of G. **b**) Close up of data in **a**) for UAI up to 5.

Figure 12 shows the variation in Poisson's ratio (ν) versus A^U for all minerals. The shaded area in Figure 12a and 12b denotes the range $0 \leq \nu \leq 0.5$. As noted by Ting & Chen (2005), ν for anisotropic materials can have no bounds. The data show that many minerals have minimum values less than 0 and maximum values greater than 0.5. The histogram in Figure 13 shows the statistical variation in ν_{min} for all minerals: 28% (=70/246) have negative minimum values for Poisson's ratio – that is, they display auxetic behaviour. Analysis of the variation of ν_{max} shows that 37% (=91/246) have values greater than 0.5 (Figure 13b). The mean value of the Voigt-Reuss-Hill average of Poisson's ratio for all minerals is 0.2464 (Figure 13c), close to the default assumption of many simplifications to elastic isotropy (ν=0.25). A full list of the rock forming minerals in our database that show auxetic behaviour is shown in Table 2, and the specific directions of negative ν are shown for several examples in the stereograms in Figure 14.

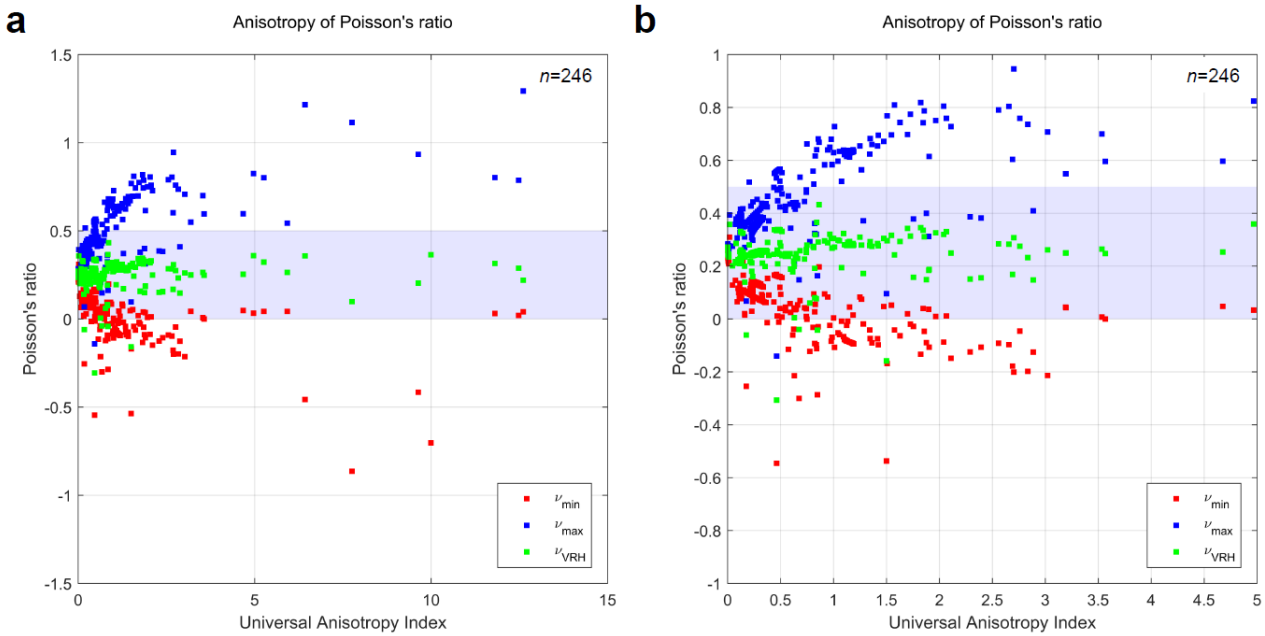

Figure 12. a) Anisotropy of Poisson's ratio in rock-forming minerals (n=246) plotted against the Universal Anisotropy Index of Ranganathan & Ostoja-Starzewski (2008). ν_{VRH} is the Voigt-Reuss-Hill average of ν. **b**) Close up of data in **a**) for UAI up to 5.

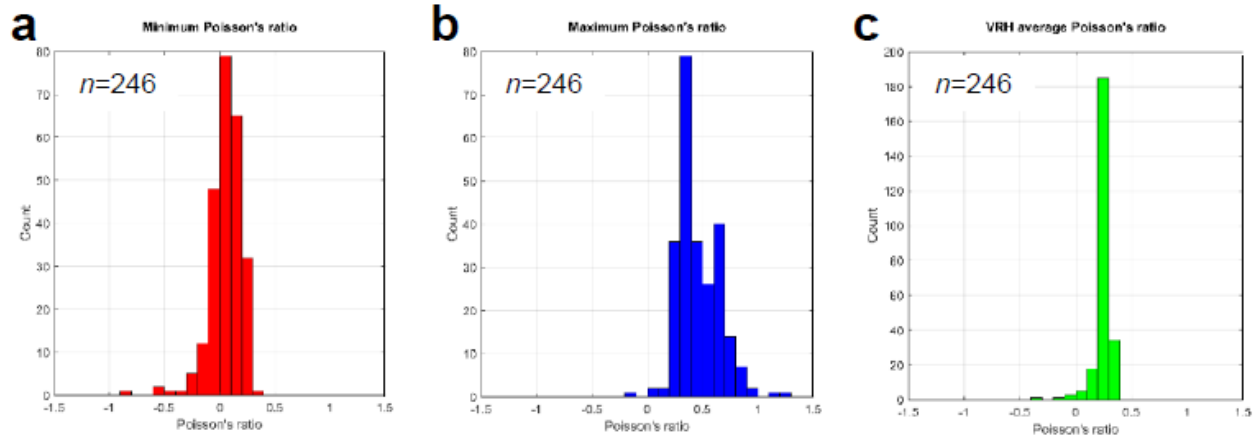

Figure 13. a) Histogram of ν_{min} values shown in Figure 12. Note that 28% (n=70/246) of minerals

483 display negative ν_{min}. **b**) Histogram of ν_{max} values. 37% (n=91/246) minerals display $\nu_{max} > 0.5$. **c**)
484 Histogram of ν_{VRH} values. Mean $\nu_{VRH} = 0.2464$, very close to the common default assumption of ν
485 = 0.25.

486

Mineral	**Symmetry**	**Minimum $\nu < 0$**	**Minimum areal $\nu < 0$**	**Reference**
Albite (An0)	Triclinic	-0.03		Hearmon, 1984
	Triclinic	-0.15		Brown et al., 2016
Anhydrite	Orthorhombic	-0.046		Hearmon, 1979
Andesine (An37)	Triclinic	-0.091		Brown et al., 2016
Andesine (An48)	Triclinic	-0.075		Brown et al., 2016
Antigorite	Monoclinic	-0.215		Bezacier et al., 2010
Aragonite	Orthorhombic	-0.061		Hearmon, 1979
Augite	Monoclinic	-0.012		Alexandrov et al., 1964
Bytownite (An78)	Triclinic	-0.053		Brown et al., 2016
Calcite	Trigonal	-0.047		Babuska & Cara, 1991
	Hexagonal	-0.02		Chen et al., 2001
Coesite	Monoclinic	-0.108		Weidner & Carleton, 1977
α-Cristobalite	Tetragonal	-0.537	-0.262	Pabst & Gregorova, 2013
β-Cristobalite	Cubic	-0.288	-0.162	Pabst & Gregorova, 2013
Dolomite	Trigonal	-0.064		Hearmon, 1979
Hornblende	Monoclinic	-0.075		Hearmon, 1984
Illite-Smectite	Monoclinic	-0.416		Militzer et al., 2011
Labradorite	Triclinic	-0.085		Ryzhova, 1964
Labradorite (An60)	Triclinic	-0.009		Brown et al., 2016
Labradorite (An67)	Triclinic	-0.025		Brown et al., 2016
Lawsonite	Orthorhombic	-0.088		Sinogeikin et al., 2000
Microcline	Triclinic	-0.199	-0.042	Babuska & Cara, 1991
Oligoclase (An25)	Triclinic	-0.098		Brown et al., 2016
Orthoclase	Monoclinic	-0.169		Hearmon, 1984
	Monoclinic	-0.092		Waeselmann et al., 2016
α-Quartz	Trigonal	-0.97	-0.071	Ogi et al., 2006
	Trigonal	-0.93	-0.067	Babuska & Cara, 1991
T=200°C	Trigonal	-0.123	-0.088	Lakshtanov et al., 2007
T=400°C	Trigonal	-0.215	-0.138	Lakshtanov et al., 2007
T=500°C	Trigonal	-0.301	-0.186	Lakshtanov et al., 2007
T=573°C	Trigonal	-0.546	-0.398	Lakshtanov et al., 2007
T=575°C	Hexagonal	-0.255	-0.095	Lakshtanov et al., 2007
Rutile	Tetragonal	-0.044		Manghnani, 1969
Sanidine	Monoclinic	-0.097		Waeselmann et al., 2016
Sillimanite	Orthorhombic	-0.001		Verma, 1960
Sphalerite	Cubic	-0.025		Hearmon, 1984
Spinel	Cubic	-0.07		Hearmon, 1984

T=300°K	Cubic	-0.081		Anderson & Isaak, 1995
T=350°K	Cubic	-0.079		Anderson & Isaak, 1995
T=400°K	Cubic	-0.083		Anderson & Isaak, 1995
T=450°K	Cubic	-0.083		Anderson & Isaak, 1995
T=500°K	Cubic	-0.084		Anderson & Isaak, 1995
T=550°K	Cubic	-0.084		Anderson & Isaak, 1995
T=600°K	Cubic	-0.085		Anderson & Isaak, 1995
T=650°K	Cubic	-0.033		Anderson & Isaak, 1995
T=700°K	Cubic	-0.088		Anderson & Isaak, 1995
T=750°K	Cubic	-0.089		Anderson & Isaak, 1995
T=800°K	Cubic	-0.09		Anderson & Isaak, 1995
T=850°K	Cubic	-0.092		Anderson & Isaak, 1995
T=900°K	Cubic	-0.093		Anderson & Isaak, 1995
T=950°K	Cubic	-0.094		Anderson & Isaak, 1995
T=1000°K	Cubic	-0.095		Anderson & Isaak, 1995
Staurolite	Orthorhombic	-0.201		Hearmon, 1979
Stishovite	Tetragonal	-0.04		Babuska & Cara, 1991
Talc (c1)	Triclinic	-0.864	-0.287	Mainprice et al., 2008
P=0.87 GPa	Triclinic	-0.178	-0.001	Mainprice et al., 2008
P=1.96 GPa	Triclinic	-0.107		Mainprice et al., 2008
P=3.89 GPa	Triclinic	-0.009		Mainprice et al., 2008
Talc (c2c)	Monoclinic	-0.126	-0.029	Mainprice et al., 2008
P=0.15 GPa	Monoclinic	-0.107	-0.021	Mainprice et al., 2008
P=0.35 GPa	Monoclinic	-0.125	-0.025	Mainprice et al., 2008
P=0.64 GPa	Monoclinic	-0.091	-0.002	Mainprice et al., 2008
P=0.93 GPa	Monoclinic	-0.028		Mainprice et al., 2008
P=1.72 GPa	Monoclinic	-0.019		Mainprice et al., 2008
Zircon (metamict)	Tetragonal	-0.113		Hearmon, 1984
Zoisite	Orthorhombic	-0.014		Mao et al., 2007
Number of distinct minerals		n=33	n=7	

Table 2. List of rock forming minerals showing auxetic behaviour (Poisson's ratio < 0) in at least one direction. Also shown are those minerals with directions that have negative areal Poisson's ratio (Guo & Wheeler, 2006). The Reference column shows the source of the elasticity data for each mineral used in the calculation. The auxetic directions were found by calculating Poisson's ratio for every possible direction (α, β, θ in the Turley & Sines reference frame shown in Figure 1) using an angular increment of 1 degree in each direction.

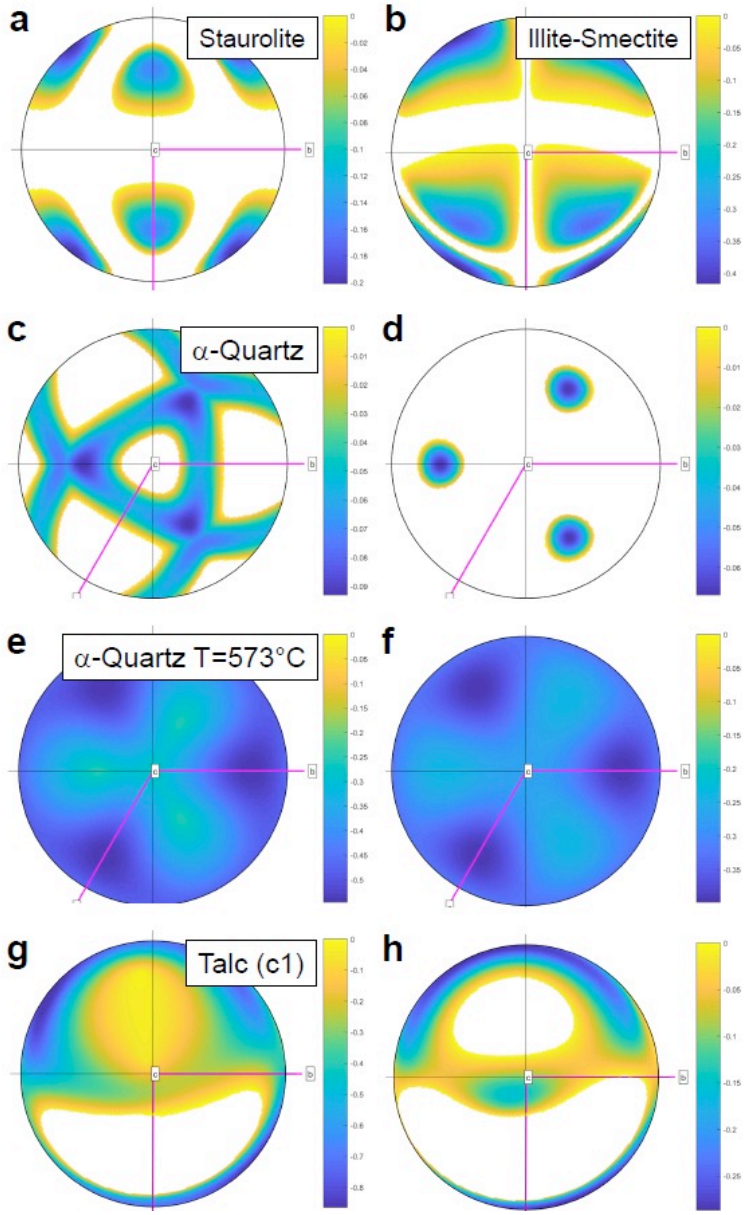

Figure 14. Examples of rock forming minerals showing auxetic and areally auxetic behaviour. Stereograms are all lower hemisphere, equal area projections and only the directions with negative Poisson's ratio (a, b, c, e, g) or negative areal Poisson's ratio (d, f, h) are shown coloured in (i.e. other directions show positive values). Crystallographic axes in pink. **a**) Staurolite. **b**) Illite-smectite. **c-d**) α-Quartz. **e-f**) α-Quartz at the temperature of the phase transformation to β-Quartz (hexagonal). **g-h**) Talc (c1, triclinic).

The elastic properties of minerals are known to be temperature (T) and pressure (P) dependent. However, systematic data to quantify the variation of anisotropic elasticity with T or P is relatively scarce. We summarise some of the published data in Figure 15, shown as the calculated range in Poisson's ratio (ν_{min} to ν_{max}). In terms of pressure dependence, the effect of increasing P is to decrease the anisotropy in ν for talc to within the range normally expected for isotropic minerals. The opposite effect is observed for zircon, with modest increases in ν_{max} with P. The temperature dependence of elastic anisotropy in quartz is well known (Mainprice & Casey, 1990), with a

significant excursion into auxetic behaviour at the temperature of the α-β phase transition at 573°C (846°K). The effect of increasing T on the anisotropy of ν for olivine, corundum and spinel is almost non-existent.

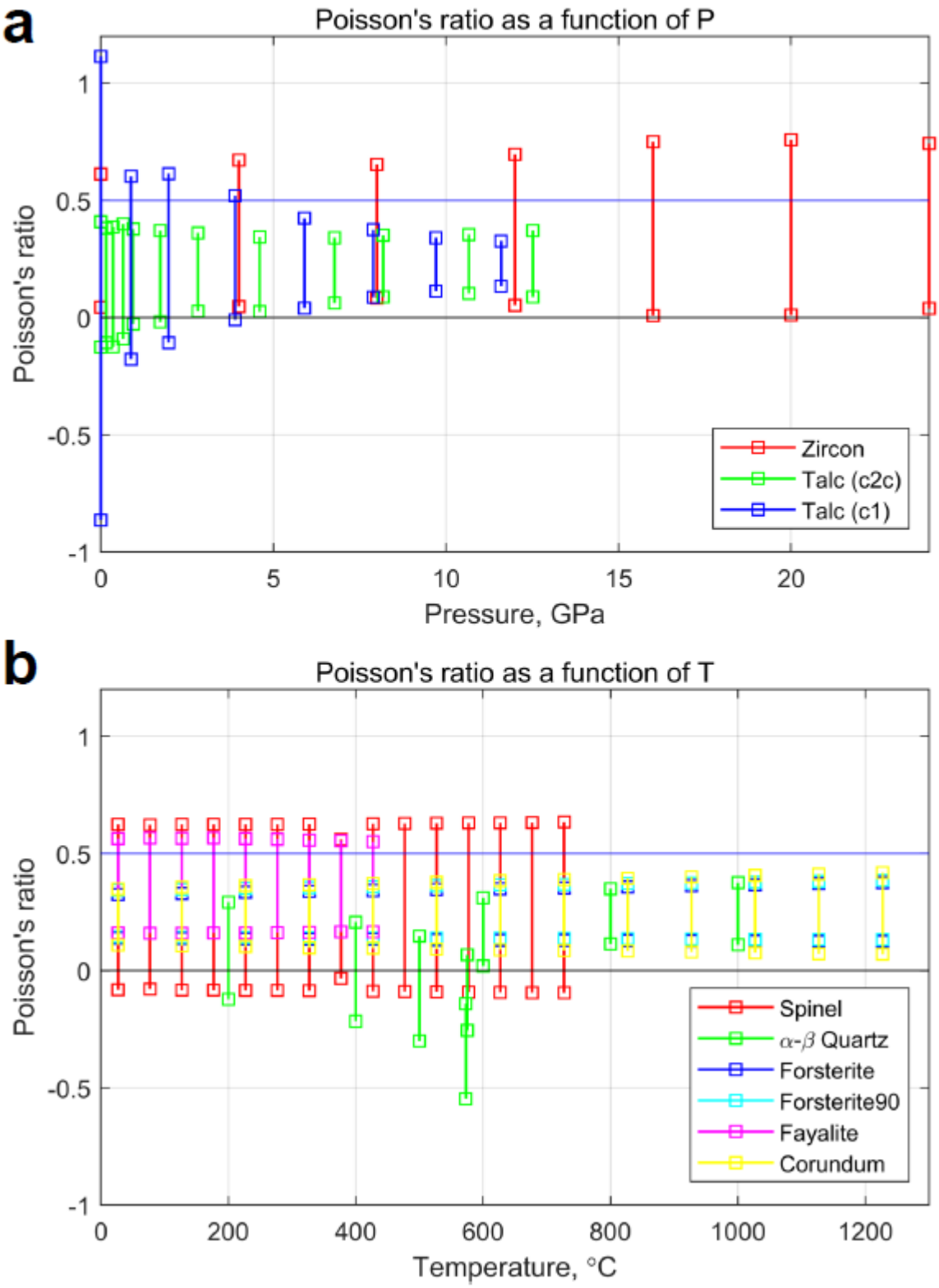

Figure 15. Anisotropy of Poisson's ratio in rock-forming minerals as a function of P (top) and T (bottom). Other than the well-known auxeticity of α-β quartz around the phase transition

(T=573°C), most minerals display Poisson's ratios of between 0-0.5. Talc (c1, triclinic) is one exception, and the anisotropy of Poisson's ratio decreases markedly with increasing P.

Linear compressibility (β) also displays significant anisotropy in rock forming minerals (Figure 17). A list of the rock forming minerals in our database that show negative linear compressibility (NLC) is shown in Table 3. These minerals have directions that expand in response to a compressive hydrostatic pressure (and vice versa: 'stretch-densification' of Baughman et al., 1998b). The specific directions of negative β are shown in the stereograms in Figure 16.

Mineral	Symmetry	Minimum $\beta < 0$, GPa^{-1}	Reference
Lizardite	Hexagonal	-0.00165	Reynard et al., 2007
Talc (c1)	Triclinic	-0.00251	Mainprice et al., 2008

Table 3. List of rock forming minerals showing negative linear compressibility (NLC) in at least one direction.

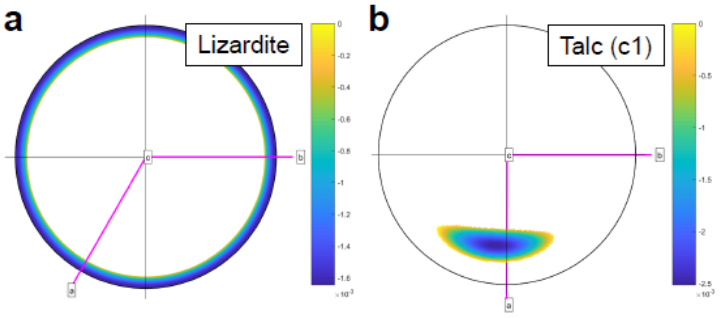

Figure 16. Rock forming minerals showing negative linear compressibility (NLC) in certain directions. Stereograms are all lower hemisphere, equal area projections and only the directions with NLC are shown coloured in (i.e. other directions show positive values). Crystallographic axes in pink. **a**) Lizardite. **b**) Talc (c1, triclinic).

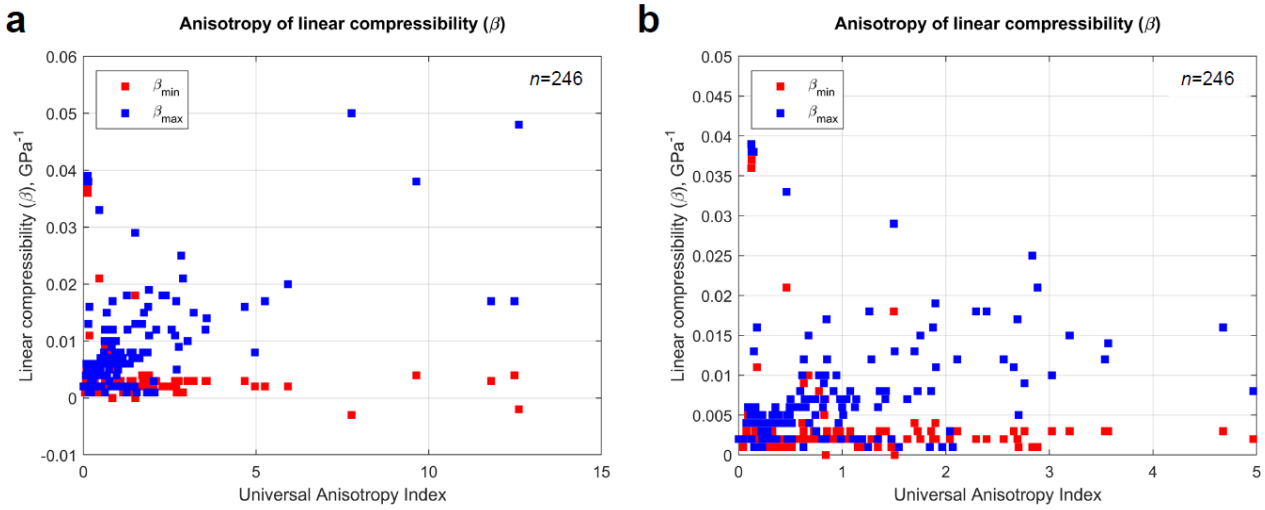

Figure 17. Anisotropy of linear compressibility in rock-forming minerals.

We can summarise the elastic anisotropy data for rock forming minerals using the Elastic Anisotropy Diagram of Ranganathan & Ostoja-Starzewski (2008). In their review of Poisson's ratio in materials, Greaves et al. (2011) used a plot of bulk modulus K versus shear modulus G, however for the anisotropic rock forming minerals there is no single value of either of these properties. We therefore take the ratios KV/KR and GV/GR and plot these instead (Figure 18). Unsurprisingly, minerals with monoclinic, triclinic and hexagonal symmetries dominate the higher anisotropies, while minerals with cubic, orthorhombic and tetragonal symmetries are generally less anisotropic.

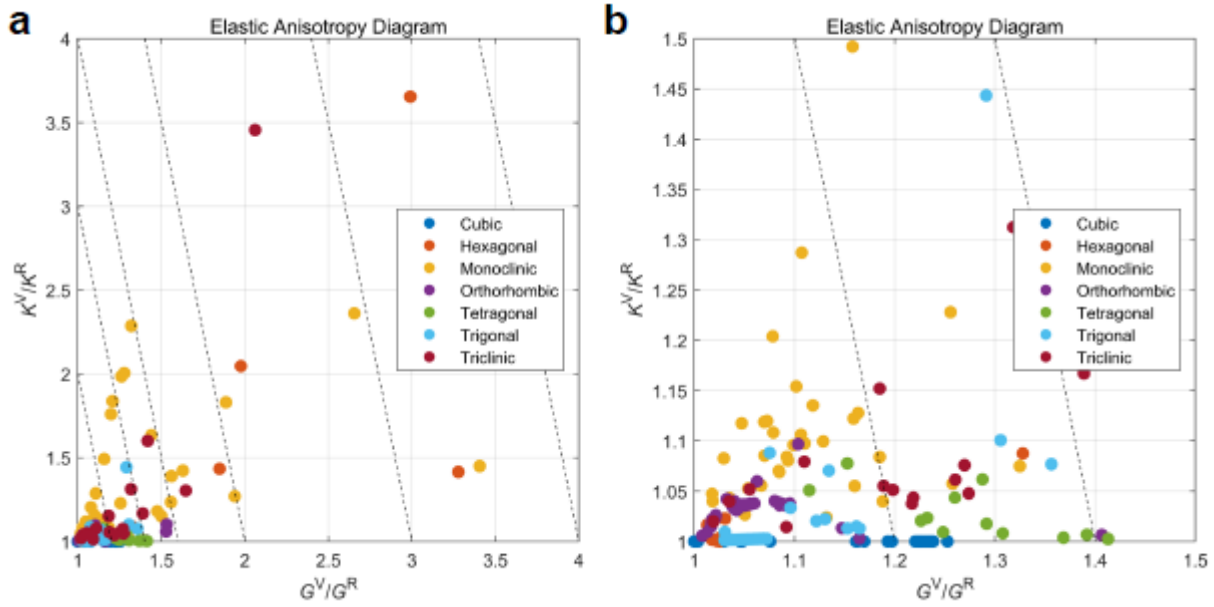

Figure 18. a) Anisotropy of rock-forming minerals (n=246) using the Elastic Anisotropy Diagram used in materials science, grouped by mineral symmetry class. **b**) Close-up of the data plotted in a), in the range G^V/G^R 1 to 1.5 and K^V/K^R 1 to 1.5.

5. Results – Specific examples

Twinning

Deformation or mechanical twinning critically depends on the anisotropy of elastic properties because minerals respond elastically to imposed stress (or strain) before exceeding the threshold for twin nucleation and propagation (Christian and Mahajan, 1995, and references therein). Perhaps the most widely accepted theory is that twin initiation occurs when an applied shear stress along the twin shear plane (K_1) in the shear direction of twinning (η_1) reaches a critical value (critically resolved shear stress, CRSS) for twin nucleation and propagation, analogous to Schmid's law for dislocation slip (Thompson and Millard, 1952; Bell and Cahn, 1953; Christian and Mahajan, 1995). However, experimental results can indicate that twinning dynamics can be more complex (e.g., Bell and Cahn, 1957). Additional complexities, such as energy barriers for the nucleation of coeval defects such as stacking faults, disconnections, and unstable transition states associated with twinning, have also been considered for twinning in metals (e.g., Serra & Bacon; 1996; Kibey et al., 2007; Pond et al., 2016). Development of a general theory of mechanical twinning applicable to most minerals is still lacking. Nevertheless, shear modulus G in η_1 along K_1 is highly relevant to mechanical twinning.

Dauphiné twins in α-quartz are merohedral twins, meaning only some atoms exchange their positions, resulting in a host-twin symmetry relationship that can be described simply by a 180° rotation about the c-axis, and recognisable in EBSD maps via a 60° misorientation around the c-axis. The formation of Dauphiné twins has been related to the difference in elastic strain energy between twinned and un-twinned at constant stress (Thomas & Wooster, 1951; Tullis, 1970; De Vore, 1970). This difference in elastic strain energy can be written as

$$\Delta E = \tfrac{1}{2} (\sigma_1 - \sigma_3)^2 \, \Delta s_{11}' \qquad (15)$$

where $(\sigma_1 - \sigma_3)$ is the applied differential stress, and $\Delta s_{11}' = s_{11}'_{\text{twinned}} - s_{11}'_{\text{un-twinned}}$. Note that s_{11}' is the reciprocal of the Young's modulus for a given direction. Dauphiné twinning occurs more readily in those directions for which the strain energy difference (ΔE) is larger, under a boundary condition of constant axial stress (the inverse is also true: under a condition of constant strain, the preferred directions of twinning are those that minimise ΔE (Paterson, 1973)). The variation of $\Delta s_{11}'$ with direction in α-quartz is shown in Figure 19. The stereogram is the same pattern shown in Thomas & Wooster (1951; their Figure 3a) and Tullis (1970; her Figure 2b). Also shown is a 3D representation surface of $\Delta s_{11}'$, which emphasises the anisotropy of favoured directions for Dauphiné twins in α-quartz. The significance of Dauphiné twinning in quartz has recently been described for sandstones compacted during diagenesis (Mørk and Moen, 2007), deformed in fault damage zones (Olierook et al., 2014), and deformed by meteorite impact (Wenk et al., 2011; Timms et al., 2019; Cox et al., 2019), and granitoid protomylonites (Menegon et al., 2011). In all cases, Dauphiné twins can be used to infer palaeostresses from deformed microstructures. In addition, Menegon et al. (2011) make the point that Dauphiné twins, formed early in a deformation history, may effectively store strain energy which is then consumed in later plastic deformation mechanisms. De Vore (1970) plotted the directional variation of compliances for quartz, ortho- and clino-pyroxene, hornblende and plagioclase and thereby extended the initial concept of Thomas & Wooster (1951). To our knowledge, detailed analyses of mechanical twins in these phases has not yet been related to the anisotropy of elastic compliance or the calculated variations in elastic strain energy for specific applied loads.

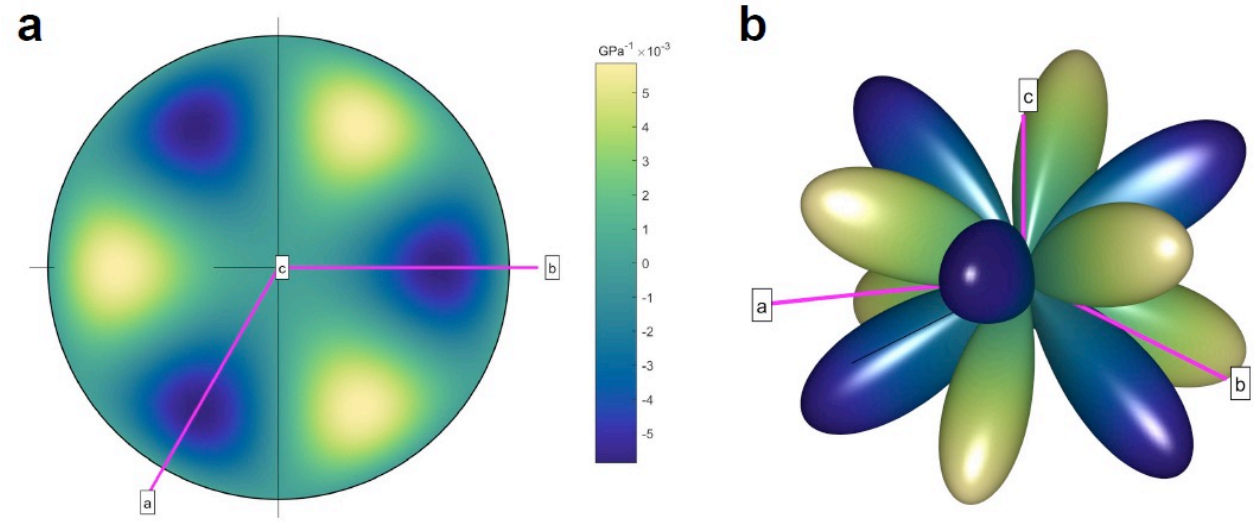

Figure 19. Anisotropy of $\Delta s_{11}'$ for Dauphiné twinning in α-quartz. $\Delta s_{11}'$ is the difference in the compliance s_{11}' between the twinned and un-twinned orientations for each direction. **a**) Stereogram (lower hemisphere, equal area projection) and **b**) a 3D representation surface, both with the

crystallographic reference axes marked. The directions represented by pale yellow/green colours will be favoured for twinning, whereas the directions shown in blue will not.

The relationship between elastic anisotropy and deformation twinning has been investigated in zircon (Timms et al., 2018). In zircon, deformation twins can form as a response to shock conditions and are diagnostic of hypervelocity impact events (Timms et al., 2012; 2017; Erickson et al. 2013). Shock twinning in zircon, which is tetragonal, can occur in up to four symmetrically equivalent orientations, forming along {112} composition planes (the of invariant shear, or K_1), and with shear direction η_1 = <111>, resulting in a host-twin 65° / {110} misorientation relationship (Timms et al., 2018). Twinning in this mode has been shown to correspond to the lowest values of G ($G_{min} = G_{<111>}$ = ~98 GPa) (Timms et al., 2018). Furthermore, the lowest values of ν are along <111> in zircon, indicating that zircon is almost perfectly compressible in <111> ($\nu_{min} = \nu_{<111>} > 0$ and <<0.1) (Timms et al., 2018). These authors illustrate that elastic softness in shear (low G) and a lack of lateral strain in the shear plane ($\nu \sim 0$) are favorable conditions for twinning in zircon (Timms et al. 2018). However, further work is required to determine the critically-resolved shear stress for twinning in zircon. Nevertheless, the ability to calculate and visualize anisotropic elastic properties in specific crystallographic directions presented here will be very useful for detailed investigations of mechanical twinning in other phases.

Polymorphic phase transformations

Coherent phase transformations (or transitions) may also be related to the anisotropy of elastic properties, including the α-β transformation in quartz. Coe & Paterson (1969) describe experiments on oriented cores from single crystals of quartz heated to temperatures above the transformation temperature (573°C, at atmospheric pressure), and subjected to non-hydrostatic stress. They found that the temperature of transition was raised by different amounts depending on the orientation of the stress with respect to the crystal. Crystal cores stressed parallel to the *c*-axis showed the least change, whereas those loaded in the *m*-direction (perpendicular to *c*) showed the greatest increase (they also performed experiments on samples cored in the *o* and *r*' directions). The temperature of phase transformation from α- (trigonal) to β- (hexagonal) quartz is therefore stress dependent. The theoretical analysis of Coe & Paterson (1969, their Appendix C) ascribes this dependence to an infinitesimal reversible transformation strain, based on the formalism of Eshelby (1957, 1959). Noting that the transformation is also marked by a '*dramatic increase in the development of small-scale Dauphine twins*', we have calculated the elastic strain energy per unit volume for each of the four core orientations tested by Coe & Paterson, using their values of applied stress (σ_1 = 1 GPa, $\sigma_2 = \sigma_3$ = 300 MPa; all compressive) and the elastic constants of α-quartz at 500°C (Lakshtanov et al., 2007). The results are shown in Figure 20, and clearly show an exact correlation with experimental data: the sample loaded in the *m* direction has the highest strain energy, and that in the *c* direction has the lowest. The overall sequence is $W(m) > W(r') > W(o) > W(c)$, which precisely mirrors that of the variation in $\partial T/\partial \sigma$ listed for each direction in Coe & Paterson (1969, their Table 3). Therefore, we speculate that the mechanism of phase transformation of α- to β- quartz may be similar to that of Dauphiné twinning in α-quartz, and favoured for those directions that maximise the elastic strain energy under a constant applied stress. We also note that similar processes may occur in pyroxenes (Coe, 1970; Coe & Muller, 1973; Clement et al., 2018).

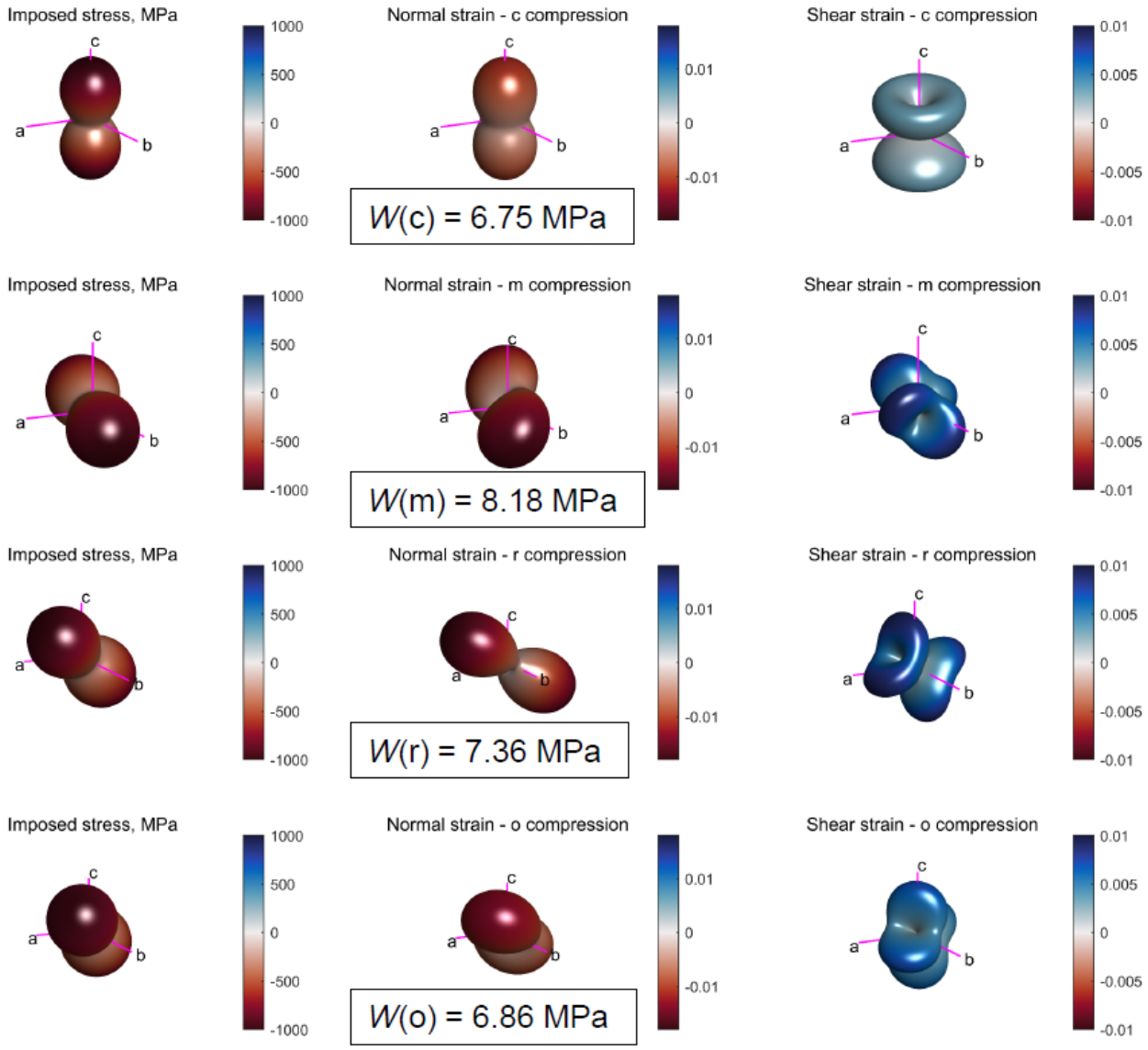

Figure 20. Variation in strain (normal and shear) and elastic strain energy for different applied loads in α-quartz at 500 °C (Lakshtanov et al. 2007). The same compressive stress (σ_1 = -1000 MPa, $\sigma_2 = \sigma_3$ = -300 MPa) is applied along the *c* (row 1), *m* (row 2), *r* (row 3), and *o* (row 4) directions in a single crystal. The Reynolds (2nd column) and HWY (3rd column) glyphs show the normal and shear strains, respectively. The elastic strain energy per unit volume (W) is shown for each configuration. Note that $W(m) > W(r) > W(o) > W(c)$.

Visualisation of elastic anisotropy has been used to gain new insights into the effects of intrinsic elastic stiffness on the transformation from zircon to the high pressure $ZrSiO_4$ polymorph reidite (Timms et al., 2018). The occurrence of lamellar reidite in shocked zircon from hypervelocity impact structures has been observed to be spatially limited to low-U domains that have not accumulated radiation damage of the lattice from the decay of U to Pb – a process known as metamictization (Cavosie et al., 2015; Erickson et al., 2017). Using elastic constants measured for variably metamict zircon (Özkan, 1976; Özkan and Jamieson, 1978), Timms et al. (2018) illustrated that the process of metamictization significantly reduces maxima of E, G and ν in zircon resulting in a compliant, isotropic structure. These authors argued that metamict domains in zircon grains are not elastically stiff enough to support sufficiently high stresses and pressures to facilitate the transformation to reidite, limiting reidite lamellae to highly crystalline non-metamict domains

during the same shock event. This finding illustrates the dependance of elastic properties on lattice defects and a potential role of intrinsic elastic properties in phase transofrmations.

Metamorphic reactions and equilibrium thermodynamics

The role of elastic deformation in the thermodynamics of preferred orientations and reactions at the scale of individual grains has long been controversial (Macdonald, 1960; Brace, 1960; Kamb, 1961 and discussion thereof; Paterson, 1973; Wheeler, 2017). Debate has centred on the role, if any, of the elastic strain energy, W. Macdonald (1960) and Brace (1960) defined the Gibbs free energy of non-hydrostatically stressed minerals in terms of the elastic strain energy, and thereby implicitly defined equilibrium under these conditions. They went on to assert that preferred orientations would develop by the (re-)orientation of a crystals in a given stress system such that their elastic strain energies were maximised. Wheeler (2017), following Kamb (1961) and Paterson (1973), asserts that there is no definable equilibrium in non-hydrostatically stressed systems. Therefore, it is wrong to equate the Gibbs energy for stressed systems of polycrystals to the elastic strain energy. Moreover, the contribution of the elastic strain energy to the chemical potentials along stressed interfaces, through the Helmholtz free energy term, is second order and therefore negligible (Wheeler, 2018).

Brittle cracking, decrepitation and dehydration

The magnitude of stresses around fluid-filled pores and cracks developed within single crystalline grains under load can be important for a variety of natural processes. The decrepitation of fluid inclusions occurs when the stresses around the pore exceed the local tensile strength, and the fluid will then drain away. Previous analyses have been rooted in linear elastic fracture mechanics, under an assumption of elastic isotropy. Similarly, in reacting systems the dehydration of hydrous phases can lead to pore fluid overpressures which crack the reacting grain and produce dehydration embrittlement (e.g. Raleigh & Paterson, 1965; Jung et al., 2004). Accurate predictions of the stress levels sustainable by intracrystalline pores and cracks are therefore vital to understanding these fundamental mechanisms. Jaeger & Cook (1969; and repeated by Pollard & Fletcher (2005)) asserted that the elastic anisotropy of rocks, measured as the ratio of Young's moduli E_{max}/E_{min}, is rarely as high as 2, and therefore the effects of elastic anisotropy are minor to negligible. Davis et al. (2017) used 3D boundary element models to show that Poisson's ratio and void (pore or crack) shape can exert significant control on the local stresses at the void-matrix boundary as a precursor to tensile or shear failure.

We have calculated the circumferential stresses around crack-like voids developed within single elastically anisotropic grains of selected minerals (Figures 21-22). The model configuration follows that of Jaeger & Cook (1969; derived from Green & Taylor, 1939), and is based on a thin 2D orthotropic plate with a single crack of aspect ratio 5:1. The assumption of orthotropy reduces the required elastic constants to five (E_1, E_2, G, ν_{21}, ν_{12}). We calculated the appropriate values of E, G and ν from polar plots of anisotropy for the [010] crystallographic plane in each mineral using AnisoVis (see Figure 4d, 5d, 5e-f). For an applied uniaxial tensile load (σ_0 in Figure 21) and a plane strain assumption, the resulting anisotropy of circumferential stress ($\sigma_{\theta\theta}$) at the void-matrix boundary is shown for four different minerals in Figure 22. Each polar plot shows the $\sigma_{\theta\theta}$ normalised by the applied load σ_0 in the [010] plane, and for two different configurations of the anisotropy with respect to the load: σ_0 parallel to the direction of E_{max} (red curves), and

perpendicular to the direction of E_{max} (blue curves). For both of the hydrous sheet silicates talc (c1; Mainprice et al., 2008) and lizardite (Reynard et al., 2007), the stresses display significant anisotropy (Figure 22a and b), with amplifications of 6-7 times the stress predicted by assuming the crystal is isotropic (black curves, calculated with VRH averages of E and ν). These stresses are likely significant for the failure of cracks or narrow fluid-filled pores in dehydrating subducting slabs (Healy et al., 2009; Ji et al., 2018). For the two feldspar examples, albite (Brown et al., 2016) and sanidine (Waeselmann et al., 2016), the amplification of circumferential stress is also significant, at 4-5 times the isotropic prediction. Again, these stresses imply that fluid-filled pores in phenocrysts of these phases may fail sooner than currently predicted under the assumption of elastic isotropy. The restriction to 2D may appear limiting in these simple illustrative models, but pending the development and analysis of fully 3D finite or boundary element models of stresses around voids in elastically anisotropic media, they can provide useful insights into the relative magnitude of local stresses and brittle failure. Moreover, we refute the suggestion from Jaeger & Cook (1969) that as the anisotropy of Young's modulus in rocks is low, the anisotropy of stresses around pores and cracks is therefore unimportant.

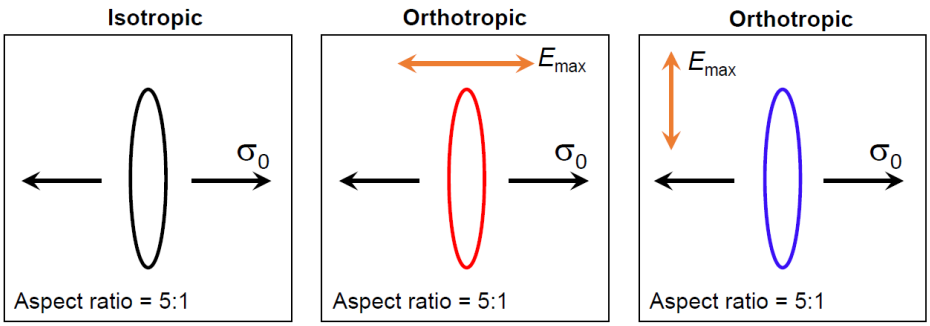

Figure 21. Schematic outline for models of narrow cracks in thin 2D orthotropic plates. The crack is subjected to a uniaxial tensile stress, and plane strain is assumed. The colours of the crack outlines correspond to the circumferential stress predictions in Figure 22.

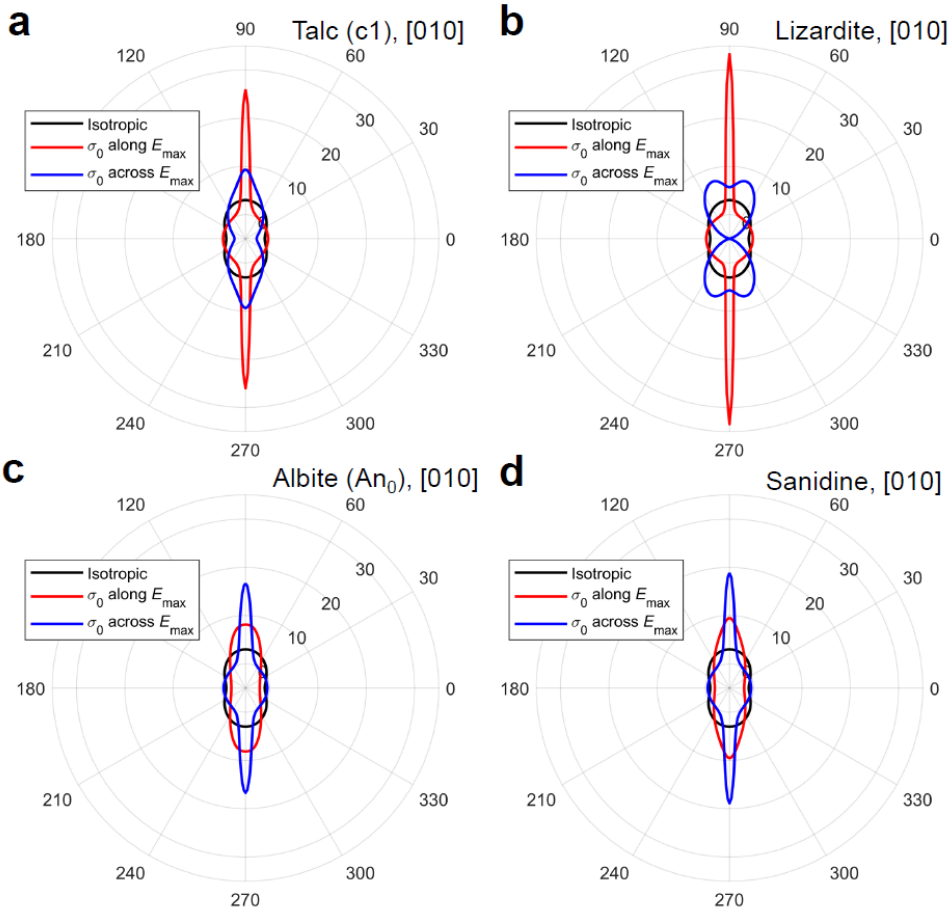

Figure 22. Predictions of stresses around cracks in thin 2D orthotropic plates. Curves show the directional variations in the circumferential stress ($\sigma_{\theta\theta}$) normalised by the applied uniaxial tensile load (σ_0). **a**) Talc (c1, triclinic), [010] plane. **b**) Lizardite, [010] plane. **c**) Albite, [010]. **d**) Sanidine, [010].

6. Summary

We reiterate a key point made by Marmier et al. (2010) in their analysis of chemical compounds: it's only by visualising elastic anisotropies, preferably in 3D, that we can truly perceive them and quantify their directions; this then allows us to relate these elastic properties to the underlying crystal structure and explore the consequences for their behaviour. In developing AnisoVis and using it to quantify the anisotropy of a specific mineral, we have presented multiple alternative visualisations of the directional variation of commonly used elastic properties such as Young's modulus (E), Poisson's ratio (ν), shear modulus (G) and linear compressibility (β). Used in combination, these depictions serve to increase our understanding of the relationships between the anisotropy of elastic properties and the underlying crystal symmetry and structure. We note that the existence of directions with negative Poisson's ratios and negative linear compressibilities in certain minerals (previously unreported). A potentially important consequence of these findings is that there must also be specific directions along which these properties – Poisson's ratio or linear compressibility – are 0. These directions will form surfaces in 3D which represents the boundary between a) domains of positive and negative Poisson's ratio (both 'regular' and areal), along which a uniaxially applied load will produce no lateral strain; and b) domains of positive and negative

linear compressibility, along which an applied hydrostatic load will produce no shortening or stretching. These surfaces and directions in rock forming minerals may yet lead to new discoveries in the physical behaviour of natural systems and novel applications in materials science or engineering (e.g. Wu et al., 2015).

Considering the results from the database of 246 sets of elastic properties, we observe that:

- significant elastic anisotropy of rock forming minerals is much **more common** than previously reported e.g. many minerals – 33 of the 86 we analysed – have auxetic directions, and some are areally auxetic;
- the elastic anisotropy of rock forming minerals is **wider** than previously reported, with widely assumed 'natural limits' frequently exceeded e.g. Poisson's ratio for many minerals is either < 0 or > 0.5.

For specific minerals, we also observe that

- elastic anisotropy has consequences for intracrystalline stresses under applied strain (and vice versa); the difference between an assumption of isotropy and using the full elastic anisotropy is often of the order of tens of MPa (even for small strains) – i.e. likely to be significant for the deformation around voids such as pores and cracks, especially in dehydrating or decrepitating systems;
- elastic anisotropy is important for mechanical (deformation) twining, especially Dauphiné twinning in quartz but probably in other minerals too;
- coherent phase transformations, such as the α-β transition in quartz, show a clear correlation with the magnitude of elastic strain energy per unit volume and the stress dependence of the transition temperature.

Further work

We are not currently limited by data; we need to process the elasticity data we have and use it to improve our understanding of Earth processes. In theoretical terms, perhaps the biggest advance would come from a solution to the Eshelby problem for an anisotropic inclusion in an anisotropic host, for ellipsoids of general shape and orientation, for the points inside and outside the inclusion. This problem is non-trivial but would be of direct relevance to the inclusion-host studies estimating pressure histories, and for mechanical problems involving voids and cracks in anisotropic crystals, including reacting systems. Numerical modelling studies of the deformation around voids and cracks might usefully incorporate a wider range of values of E and ν. Visualisation of direction-specific elastic properties will be useful for future investigations of the mechanics of twinning, dislocations, and fractures in a wide range of minerals. Earthquake focal mechanisms are known to depend on the elastic anisotropy of the source region (Vavrycuk, 2005), and better understanding of the anisotropies in rock forming minerals is informing models of fabrics in subducting slabs (Li et al., 2018) and interpretations of microseismicity from commercial hydraulic fracturing operations (Jia et al., 2018). A practical assessment of the contribution of elastic strain energy to metamorphic reactions might involve the systematic mapping of major element chemistry around specific inclusions.

We believe that publicly available and easy-to-use software tools like AnisoVis may be useful in teaching environments to guide understanding of the links between mineral properties (elastic,

acoustic, optical) and their underlying symmetry and lattice structure. Following Nye's original text, other properties such as piezolectric and thermal conductivities, could also be added and visualised (Tommasi, 2001; Mainprice et al., 2015). Our AnisoVis MATLAB source code and sample elasticity files have been made available in open repositories so that other developers and researchers will optimise and extend the functionality, and that "given enough eyeballs, all bugs are shallow" (Raymond, 1999).

Acknowledgements

DH thanks John Wheeler (Liverpool) for discussion, and Ross Angel (Padua) for a reprint. This paper is dedicated to the memory of John Frederick Nye (1923-2019) whose seminal text book, first published in 1957 (Physical Properties of Crystals: Their Representation by Tensors and Matrices; reprinted as Nye, 1985), has been a huge influence on the lead author. DH acknowledges financial support from NERC (UK), grant NE/N003063/1.

Appendix A – benchmarks to previously published anisotropic elastic properties

The outputs from AnisoVis, and the calculations underlying them, have been benchmarked against previously published examples, chiefly from chemistry and materials science literature. Figures produced by AnisoVis are shown below, with one example per symmetry group, formatted to mimic the plots in the original publication.

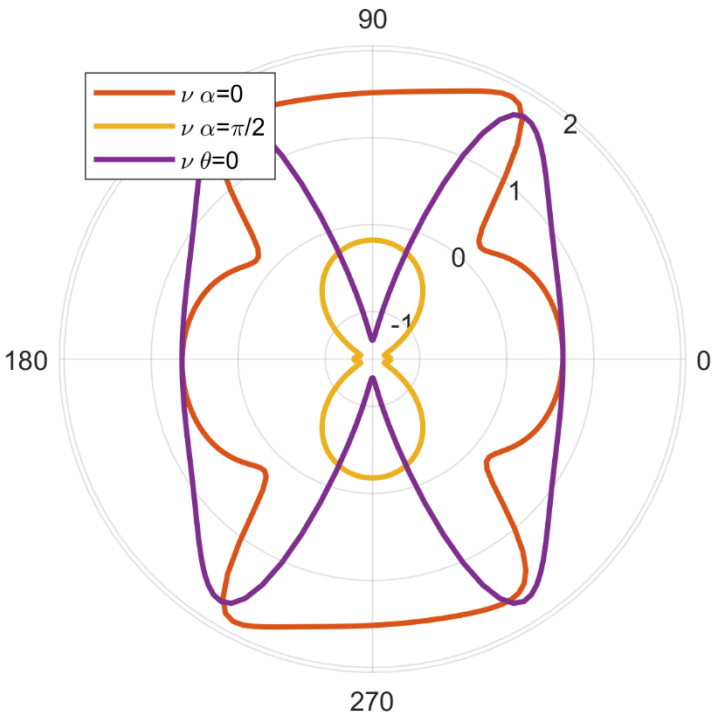

Figure A1. Benchmarks to Rovati (2004, their Figure 4) for monoclinic cesium dihydrogen phosphate. Note the extreme auxeticity (negative Poisson's ratio) shown by this material.

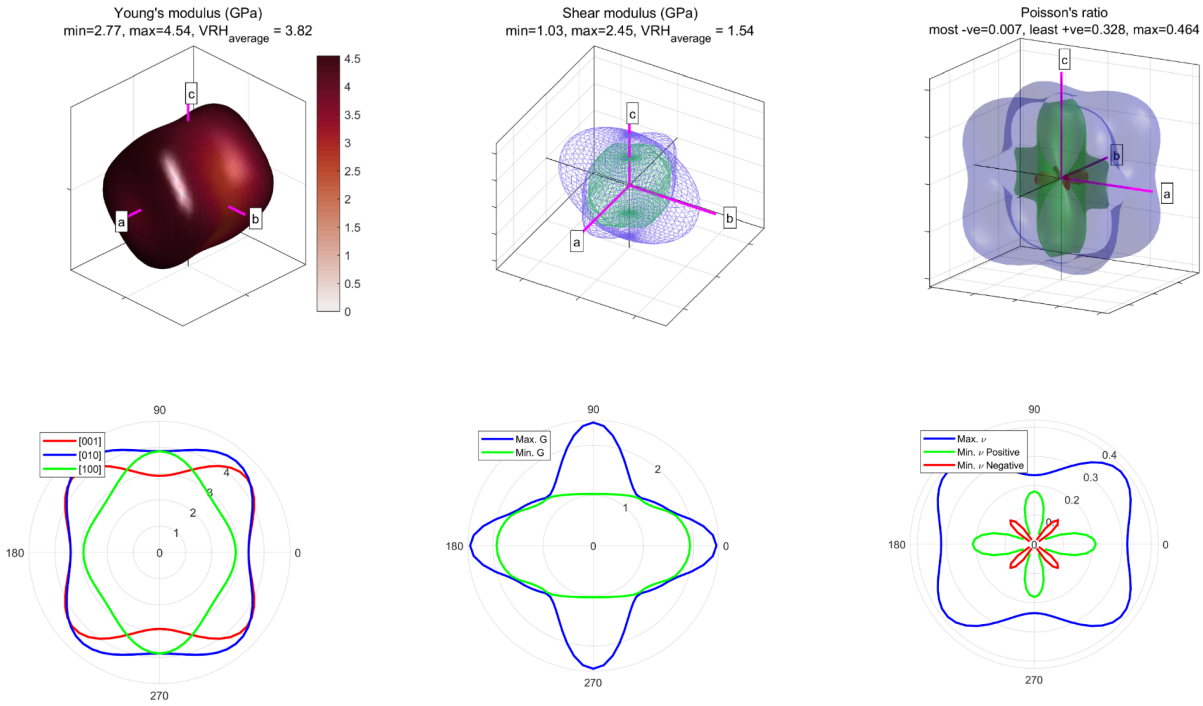

803 **Figure A2.** Benchmarks to Tan et al. (2015, their Figures 2, 3 and 4) for orthorhombic ZIF-4, a
804 zeolite. Plots shown for Young's modulus, shear modulus and Poisson's ratio.

805

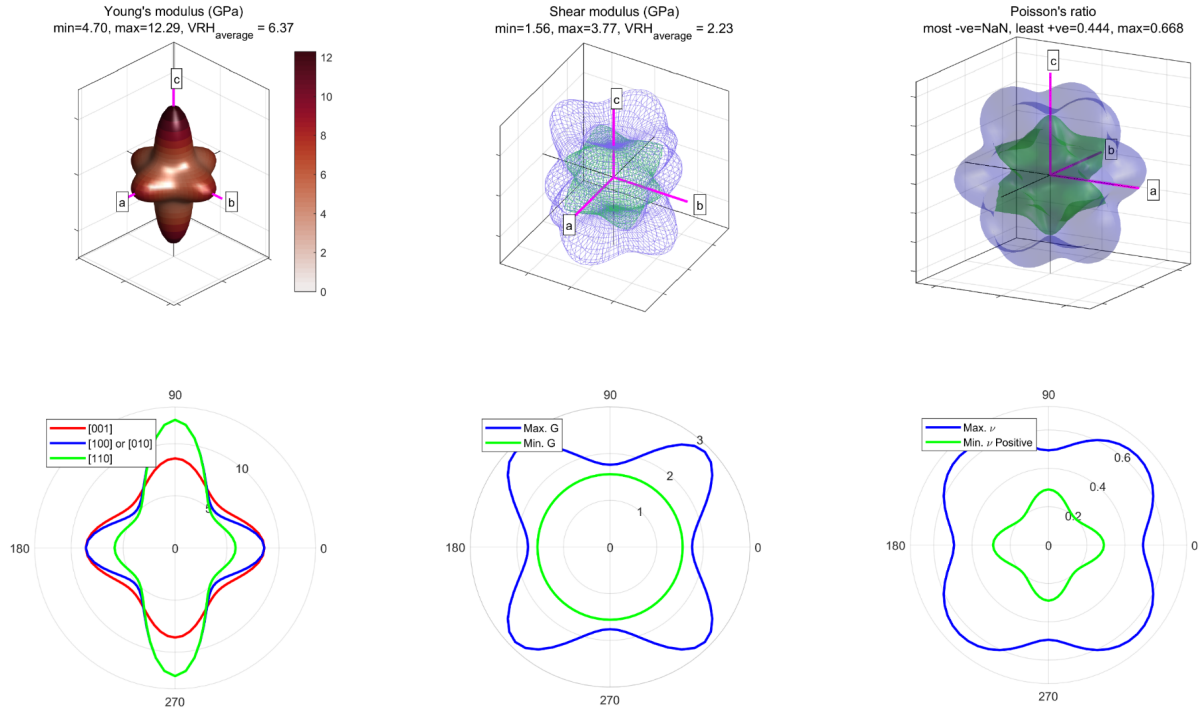

806 **Figure A3.** Benchmarks to Tan et al. (2015, their Figures 2, 3 and 4) for tetragonal ZIF-zni, a
807 zeolite. Plots shown for Young's modulus, shear modulus and Poisson's ratio.

808

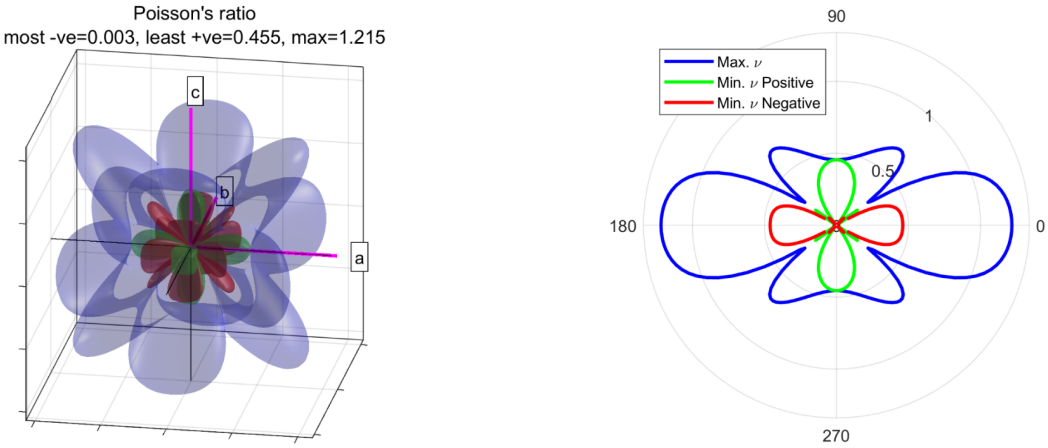

809 **Figure A4.** Benchmarks to Marmier et al. (2010, their Figure 5 and 6) for cubic cesium. Note the
810 auxetic nature of Poisson's ratio.

811

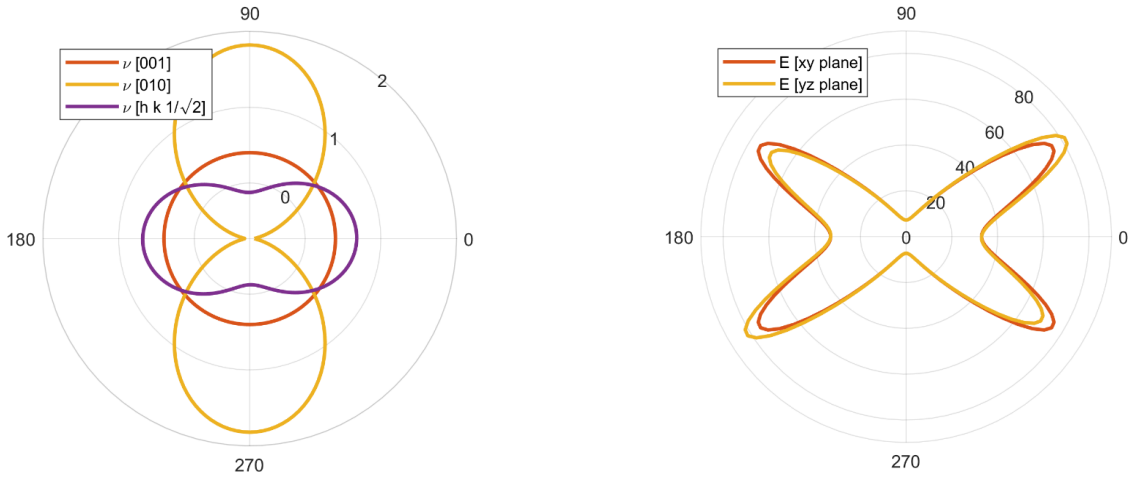

812 **Figure A5.** Benchmarks to Gunton & Saunders (1972, their Figures 3 and 6) for trigonal arsenic.

813

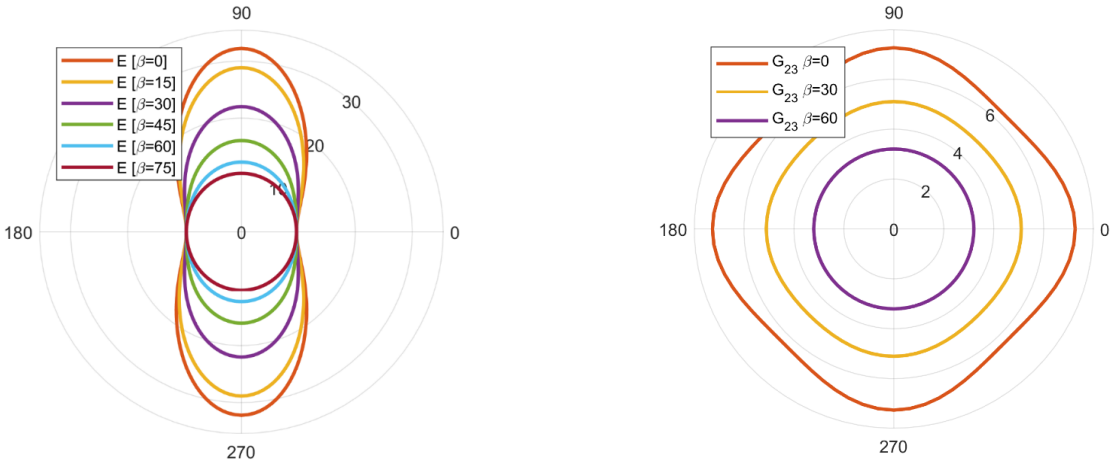

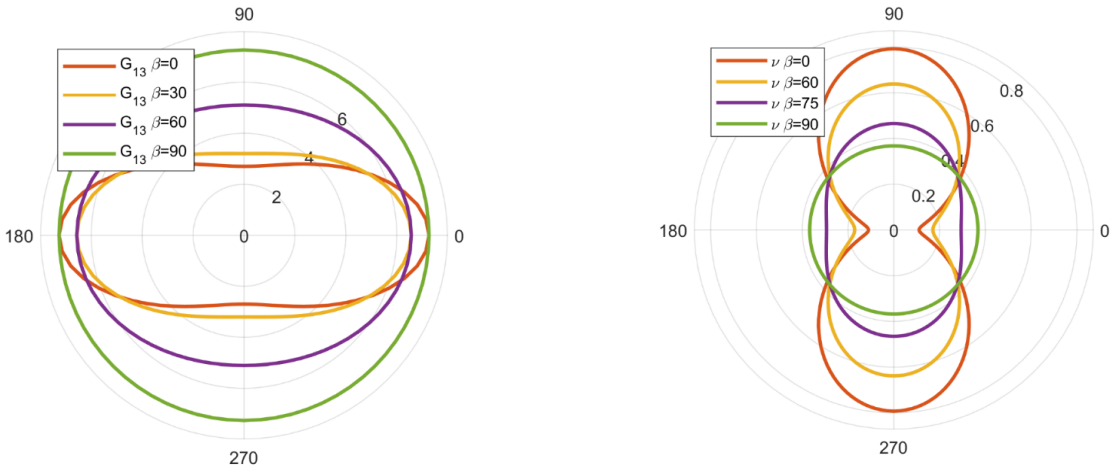

814 **Figure A6.** Benchmarks to Li (1976, their Figure 3) for hexagonal thallium.

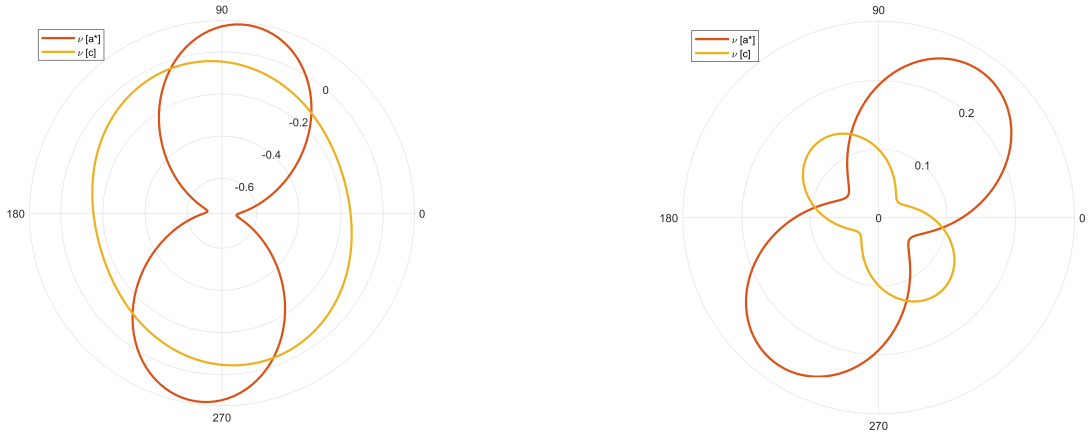

815 **Figure A7.** Benchmarks to Mainprice et al. (2008, their Figure 5) for triclinic talc (c1) at 0.0 GPa
816 (left) and 3.9 GPa (right). The lower pressure example shows auxetic behaviour.

817

818 **References**

819 Aleksandrov, K.S., Ryzhova, T.V. & Belikov, B.P. 1964. The elastic properties of pyroxenes.
820 Soviet Physics Crystallography, 8, pp.589-591.

821 Almqvist, B.S. & Mainprice, D., 2017. Seismic properties and anisotropy of the continental crust:
822 predictions based on mineral texture and rock microstructure. Reviews of Geophysics, 55(2),
823 pp.367-433.

824 Anderson, O.L. & Isaak, D.G., 1995. Elastic constants of mantle minerals at high temperature.
825 Mineral physics and crystallography: a handbook of physical constants, 2, pp.64-97.

826 Angel, R.J., Mazzucchelli, M.L., Alvaro, M., Nimis, P. & Nestola, F., 2014. Geobarometry from
827 host-inclusion systems: the role of elastic relaxation. American Mineralogist, 99(10), pp.2146-2149.

828 Angel, R.J., Nimis, P., Mazzucchelli, M.L., Alvaro, M. & Nestola, F., 2015. How large are
829 departures from lithostatic pressure? Constraints from host–inclusion elasticity. Journal of
830 Metamorphic Geology, 33(8), pp.801-813.

831 Aouni, N. & Wheeler, L., 2008. Auxeticity of Calcite and Aragonite polymorphs of CaCO3 and
832 crystals of similar structure. physica status solidi (b), 245(11), pp.2454-2462.

833 Babuska, V. & Cara, M., 1991. Seismic anisotropy in the Earth (Vol. 10). Springer Science &
834 Business Media.

835 Bass, J.D., 1995. Elastic properties of minerals, melts, and glasses. Handbook of Physical
836 Constants, pp.45-63.

837 Baughman, R.H., Shacklette, J.M., Zakhidov, A.A. & Stafström, S., 1998a. Negative Poisson's
838 ratios as a common feature of cubic metals. Nature, 392(6674), p.362.

839 Baughman, R.H., Stafström, S., Cui, C. & Dantas, S.O., 1998b. Materials with negative
840 compressibilities in one or more dimensions. Science, 279(5356), pp.1522-1524.

841 Bell, R. L., & Cahn, R. W. 1953. The nucleation problem in deformation twinning. Acta
842 Metallurgica, 1(6), 752-753.

843 Bell, R. L., & Cahn, R. W. 1957. The dynamics of twinning and the interrelation of slip and
844 twinning in zinc crystals. Proceedings of the Royal Society of London. Series A. Mathematical and
845 Physical Sciences, 239(1219), 494-521.

846 Bezacier, L., Reynard, B., Bass, J.D., Sanchez-Valle, C. & Van de Moortèle, B., 2010. Elasticity of
847 antigorite, seismic detection of serpentinites, and anisotropy in subduction zones. Earth and
848 Planetary Science Letters, 289(1-2), pp.198-208.

849 Birch, A.F. & Bancroft, D., 1938. The elasticity of certain rocks and massive minerals. American
850 Journal of Science, 237(1), pp.2-6.

851 Brace, W.F., 1960. Orientation of anisotropic minerals in a stress field: discussion. Geological
852 Society of America Memoirs, 79, pp.9-20.

853 Britton, T.B., Jiang, J., Guo, Y., Vilalta-Clemente, A., Wallis, D., Hansen, L.N., Winkelmann, A. &
854 Wilkinson, A.J., 2016. Tutorial: Crystal orientations and EBSD—Or which way is up?. Materials
855 Characterization, 117, pp.113-126.

856 Brown, J.M., Angel, R.J. & Ross, N.L., 2016. Elasticity of plagioclase feldspars. Journal of
857 Geophysical Research: Solid Earth, 121(2), pp.663-675.

858 Cavosie, A. J., Erickson, T. M., & Timms, N. E. 2015. Nanoscale records of ancient shock
859 deformation: Reidite (ZrSiO4) in sandstone at the Ordovician Rock Elm impact crater. Geology,
860 43(4), 315-318.

861 Chen, C.C., Lin, C.C., Liu, L.G., Sinogeikin, S.V. & Bass, J.D., 2001. Elasticity of single-crystal
862 calcite and rhodochrosite by Brillouin spectroscopy. American Mineralogist, 86(11-12), pp.1525-
863 1529.

Chopin, C., 1984. Coesite and pure pyrope in high-grade blueschists of the Western Alps: a first record and some consequences. Contributions to Mineralogy and Petrology, 86(2), pp.107-118.

Christian, J. W., & S. Mahajan (1995), Deformation twinning, Progress in Materials Science, 39, 1–57.

Christoffel, E.B., 1877. Uber die Fortpflanzung von Stössen durch elastische feste Körper. Annali di Matematica Pura ed Applicata (1867-1897), 8(1), pp.193-243.

Clément, M., Padrón-Navarta, J.A., Tommasi, A. & Mainprice, D., 2018. Non-hydrostatic stress field orientation inferred from orthopyroxene (Pbca) to low-clinoenstatite (P 21/c) inversion in partially dehydrated serpentinites. American Mineralogist: Journal of Earth and Planetary Materials, 103(6), pp.993-1001.

Coe, R.S., 1970. The thermodynamic effect of shear stress on the ortho-clino inversion in enstatite and other coherent phase transitions characterized by a finite simple shear. Contributions to mineralogy and petrology, 26(3), pp.247-264.

Coe, R.S. and Paterson, M.S., 1969. The α–β inversion in quartz: a coherent phase transition under nonhydrostatic stress. Journal of Geophysical Research, 74(20), pp.4921-4948.

Coe, R.S. & Muller, W.F., 1973. Crystallographic orientation of clinoenstatite produced by deformation of orthoenstatite. Science, 180(4081), pp.64-66.

Cox, M.A., Cavosie, A.J., Ferrière, L., Timms, N.E., Bland, P.A., Miljković, K., Erickson, T.M. & Hess, B., 2019. Shocked quartz in polymict impact breccia from the Upper Cretaceous Yallalie impact structure in Western Australia. Meteoritics & Planetary Science, 54(3), pp.621-637.

Davis, T., Healy, D., Bubeck, A. & Walker, R., 2017. Stress concentrations around voids in three dimensions: The roots of failure. Journal of Structural Geology, 102, pp.193-207.

Deer, W., Howie, R. & Zussman, J., 1992. *An introduction to the rock-forming minerals*. Essex. England: Longman Scientific and Technology.

DeVore, G.W., 1970. Elastic compliances of minerals related to crystallographic orientation and elastic strain energy relations in twinned crystals. Lithos, 3(3), pp.193-208.

Erickson, T. M., A. J. Cavosie, D. E. Moser, I. R. Barker & H. A. Radovan. 2013a. Correlating planar microstructures in shocked zircon from the Vredefort Dome at multiple scales: Crystallographic modeling, external and internal imaging, and EBSD structural analysis, American Mineralogist, 98, 53–65.

Erickson, T. M., Pearce, M. A., Reddy, S. M., Timms, N. E., Cavosie, A. J., Bourdet, J. & Nemchin, A. A. 2017. Microstructural constraints on the mechanisms of the transformation to reidite in naturally shocked zircon. Contributions to Mineralogy and Petrology, 172(1), 6.

Eshelby, J.D., 1957. The determination of the elastic field of an ellipsoidal inclusion, and related problems. Proceedings of the Royal Society of London. Series A. Mathematical and Physical Sciences, 241(1226), pp.376-396.

Eshelby, J.D., 1959. The elastic field outside an ellipsoidal inclusion. Proceedings of the Royal Society of London. Series A. Mathematical and Physical Sciences, 252(1271), pp.561-569.

Gaillac, R., Pullumbi, P. & Coudert, F.X., 2016. ELATE: an open-source online application for analysis and visualization of elastic tensors. Journal of Physics: Condensed Matter, 28(27), p.275201.

Gercek, H., 2007. Poisson's ratio values for rocks. International Journal of Rock Mechanics and Mining Sciences, 44(1), pp.1-13.

Gillet, P., Ingrin, J. & Chopin, C., 1984. Coesite in subducted continental crust: PT history deduced from an elastic model. Earth and Planetary Science Letters, 70(2), pp.426-436.

Greaves, G.N., Greer, A.L., Lakes, R.S. & Rouxel, T., 2011. Poisson's ratio and modern materials. Nature materials, 10(11), p.823.

Green, A.E. & Taylor, G.I., 1939. Stress systems in aeolotropic plates. I. Proceedings of the Royal Society of London. Series A. Mathematical and Physical Sciences, 173(953), pp.162-172.

Gunton, D.J. & Saunders, G.A., 1972. The Young's modulus and Poisson's ratio of arsenic, antimony and bismuth. Journal of Materials Science, 7(9), pp.1061-1068.

Guo, C.Y. & Wheeler, L., 2006. Extreme Poisson's ratios and related elastic crystal properties. Journal of the Mechanics and Physics of Solids, 54(4), pp.690-707.

Hashash, Y.M., Yao, J.I.C. & Wotring, D.C., 2003. Glyph and hyperstreamline representation of stress and strain tensors and material constitutive response. International journal for numerical and analytical methods in geomechanics, 27(7), pp.603-626.

Healy, D., Reddy, S.M., Timms, N.E., Gray, E.M. & Brovarone, A.V., 2009. Trench-parallel fast axes of seismic anisotropy due to fluid-filled cracks in subducting slabs. Earth and Planetary Science Letters, 283(1-4), pp.75-86.

Hearmon, R.F.S., 1946. The elastic constants of anisotropic materials. Reviews of Modern Physics, 18(3), p.409.

Hearmon, R.F.S., 1979. The third-and higher-order elastic constants. Numerical Data and Functional Relationships in Science and Technology, Landolt-Bornstein, 11.

Hearmon, R.F.S., 1984. The elastic constants of crystals and other anisotropic materials. Landolt-Bornstein Tables, III/18, p.1154.

Hielscher, R. & Schaeben, H., 2008. A novel pole figure inversion method: specification of the MTEX algorithm. Journal of Applied Crystallography, 41(6), pp.1024-1037.

Hill, R., 1952. The elastic behaviour of a crystalline aggregate. Proceedings of the Physical Society. Section A, 65(5), p.349.

Jaeger, J.C. & Cook, N.G., 1969. *Fundamentals of rock mechanics*. Methuen & Co. Ltd., London, 513.

Ji, S., Li, L., Motra, H.B., Wuttke, F., Sun, S., Michibayashi, K. & Salisbury, M.H., 2018. Poisson's ratio and auxetic properties of natural rocks. Journal of Geophysical Research: Solid Earth, 123(2), pp.1161-1185.

Jia, S.Q., Eaton, D.W. & Wong, R.C., 2018. Stress inversion of shear-tensile focal mechanisms with application to hydraulic fracture monitoring. Geophysical Journal International, 215(1), pp.546-563.

Jung, H., Green Ii, H.W. & Dobrzhinetskaya, L.F., 2004. Intermediate-depth earthquake faulting by dehydration embrittlement with negative volume change. Nature, 428(6982), p.545.

Kamb, W.B., 1961. The thermodynamic theory of nonhydrostatically stressed solids. Journal of Geophysical Research, 66(1), pp.259-271.

Karki, B.B. & Chennamsetty, R., 2004. A visualization system for mineral elasticity. Visual Geosciences, 9(1), pp.49-57.

Kern, H., 1982. Elastic-wave velocity in crustal and mantle rocks at high pressure and temperature: the role of the high-low quartz transition and of dehydration reactions. Physics of the Earth and Planetary Interiors, 29(1), pp.12-23.

Kibey, S., J. B. Liu, D. D. Johnson & H. Sehitoglu (2007). Predicting twinning stress in fcc metals: Linking twin□energy pathways to twin nucleation, Acta Mater., 55, 6843–6851.

Kratz, A., Auer, C. & Hotz, I., 2014. *Tensor Invariants and Glyph Design. In Visualization and Processing of Tensors and Higher Order Descriptors for Multi-Valued Data* (pp. 17-34). Springer, Berlin, Heidelberg.

Lacazette, A., 1990. Application of linear elastic fracture mechanics to the quantitative evaluation of fluid-inclusion decrepitation. Geology, 18(8), pp.782-785.

Lakes, R., 1987. Foam structures with a negative Poisson's ratio. Science, 235, pp.1038-1041.

Lakshtanov, D.L., Sinogeikin, S.V. & Bass, J.D., 2007. High-temperature phase transitions and elasticity of silica polymorphs. Physics and Chemistry of Minerals, 34(1), pp.11-22.

Lethbridge, Z.A., Walton, R.I., Marmier, A.S., Smith, C.W. & Evans, K.E., 2010. Elastic anisotropy and extreme Poisson's ratios in single crystals. Acta Materialia, 58(19), pp.6444-6451.

Li, Y., 1976. The anisotropic behavior of Poisson's ratio, Young's modulus, and shear modulus in hexagonal materials. physica status solidi (a), 38(1), pp.171-175.

Li, J., Zheng, Y., Thomsen, L., Lapen, T.J. & Fang, X., 2018. Deep earthquakes in subducting slabs hosted in highly anisotropic rock fabric. Nature Geoscience, 11(9), p.696.

Lloyd, G.E. & Kendall, J.M., 2005. Petrofabric-derived seismic properties of a mylonitic quartz simple shear zone: implications for seismic reflection profiling. Geological Society, London, Special Publications, 240(1), pp.75-94.

MacDonald, G.J., 1960. Orientation of anisotropic minerals in a stress field. Geological Society of America Memoirs, 79, pp.1-8.

971 Mainprice, D., 1990. A FORTRAN program to calculate seismic anisotropy from the lattice
972 preferred orientation of minerals. Computers & Geosciences, 16(3), pp.385-393.

973 Mainprice, D. & Casey, M., 1990. The calculated seismic properties of quartz mylonites with
974 typical fabrics: relationship to kinematics and temperature. Geophysical Journal International,
975 103(3), pp.599-608.

976 Mainprice, D., Le Page, Y., Rodgers, J. & Jouanna, P., 2008. Ab initio elastic properties of talc
977 from 0 to 12 GPa: interpretation of seismic velocities at mantle pressures and prediction of auxetic
978 behaviour at low pressure. Earth and Planetary Science Letters, 274(3-4), pp.327-338.

979 Mainprice, D., Hielscher, R. & Schaeben, H., 2011. Calculating anisotropic physical properties
980 from texture data using the MTEX open-source package. Geological Society, London, Special
981 Publications, 360(1), pp.175-192.

982 Mainprice, D., Bachmann, F., Hielscher, R., Schaeben, H. & Lloyd, G.E., 2015. Calculating
983 anisotropic piezoelectric properties from texture data using the MTEX open source package.
984 Geological Society, London, Special Publications, 409(1), pp.223-249.

985 Mandell, W., 1927. The determination of the elastic moduli of the piezo-electric crystal Rochelle
986 salt by a statical method. Proceedings of the Royal Society of London. Series A, Containing Papers
987 of a Mathematical and Physical Character, 116(775), pp.623-636.

988 Manghnani, M.H., 1969. Elastic constants of single□crystal rutile under pressures to 7.5 kilobars.
989 Journal of Geophysical Research, 74(17), pp.4317-4328.

990 Mao, Z., Jiang, F. & Duffy, T.S., 2007. Single-crystal elasticity of zoisite Ca2Al3Si3O12 (OH) by
991 Brillouin scattering. American Mineralogist, 92(4), pp.570-576.

992 Marmier, A., Lethbridge, Z.A., Walton, R.I., Smith, C.W., Parker, S.C. & Evans, K.E., 2010.
993 ElAM: A computer program for the analysis and representation of anisotropic elastic properties.
994 Computer Physics Communications, 181(12), pp.2102-2115.

995 Mazzucchelli, M.L., Burnley, P., Angel, R.J., Morganti, S., Domeneghetti, M.C., Nestola, F. &
996 Alvaro, M., 2018. Elastic geothermobarometry: Corrections for the geometry of the host-inclusion
997 system. Geology, 46(3), pp.231-234.

998 Menegon, L., Piazolo, S. & Pennacchioni, G., 2011. The effect of Dauphiné twinning on plastic
999 strain in quartz. Contributions to Mineralogy and Petrology, 161(4), pp.635-652.

1000 Militzer, B., Wenk, H.R., Stackhouse, S. & Stixrude, L., 2011. First-principles calculation of the
1001 elastic moduli of sheet silicates and their application to shale anisotropy. American Mineralogist,
1002 96(1), pp.125-137.

1003 Moore, J.G., Schorn, S.A. & Moore, J., 1996. Methods of Classical Mechanics Applied to
1004 Turbulence Stresses in a Tip Leakage Vortex. Journal of turbomachinery, 118(4), pp.622-629.

1005 Mörk, M. B. E., & Moen, K. 2007. Compaction microstructures in quartz grains and quartz cement
1006 in deeply buried reservoir sandstones using combined petrography and EBSD analysis. Journal of
1007 Structural Geology, 29(11), 1843-1854.

1008 Nye, J.F., 1985. *Physical properties of crystals: their representation by tensors and matrices.*
1009 Oxford University Press.

1010 Ogi, H., Ohmori, T., Nakamura, N. & Hirao, M., 2006. Elastic, anelastic, and piezoelectric
1011 coefficients of α-quartz determined by resonance ultrasound spectroscopy. Journal of Applied
1012 Physics, 100(5), p.053511.

1013 Olierook, H. K., Timms, N. E., & Hamilton, P. J. (2014). Mechanisms for permeability
1014 modification in the damage zone of a normal fault, northern Perth Basin, Western Australia. Marine
1015 and Petroleum Geology, 50, 130-147.

1016 Özkan, H. 1976. Effect of nuclear radiation on the elastic moduli of zircon. Journal of Applied
1017 Physics, 47(11), 4772-4779.

1018 Özkan, H., & Jamieson, J. C. 1978. Pressure dependence of the elastic constants of non-metamict
1019 zircon. Physics and Chemistry of Minerals, 2(3), 215-224.

1020 Pabst, W. & Gregorová, E.V.A., 2013. Elastic properties of silica polymorphs—a review.
1021 Ceramics-Silikaty, 57(3), pp.167-184.

1022 Pasternak, E. & Dyskin, A.V., 2012. Materials and structures with macroscopic negative Poisson's
1023 ratio. International Journal of Engineering Science, 52, pp.103-114.

1024 Paterson, M.S., 1973. Nonhydrostatic thermodynamics and its geologic applications. Reviews of
1025 Geophysics, 11(2), pp.355-389.

1026 Pollard, D.D. & Fletcher, R.C., 2005. *Fundamentals of Structural Geology*. Cambridge University
1027 Press, pp.512.

1028 Pond, R. C., Hirth, J. P., Serra, A., & Bacon, D. J. 2016. Atomic displacements accompanying
1029 deformation twinning: shears and shuffles. Materials Research Letters, 4(4), 185-190.

1030 Prawoto, Y., 2012. Seeing auxetic materials from the mechanics point of view: a structural review
1031 on the negative Poisson's ratio. Computational Materials Science, 58, pp.140-153.

1032 Raleigh, C.B. & Paterson, M.S., 1965. Experimental deformation of serpentinite and its tectonic
1033 implications. Journal of Geophysical Research, 70(16), pp.3965-3985.

1034 Ranganathan, S.I. & Ostoja-Starzewski, M., 2008. Universal elastic anisotropy index. Physical
1035 Review Letters, 101(5), p.055504.

1036 Raymond, E., 1999. The cathedral and the bazaar. Knowledge, Technology & Policy, 12(3), pp.23-
1037 49.

1038 Reynard, B., Hilairet, N., Balan, E. & Lazzeri, M., 2007. Elasticity of serpentines and extensive
1039 serpentinization in subduction zones. Geophysical Research Letters, 34(13).

1040 Rosenfeld, J.L., 1969. Stress effects around quartz inclusions in almandine and the
1041 piezothermometry of coexisting aluminum silicates. American Journal of Science, 267(3), pp.317-
1042 351.

Rosenfeld, J.L. & Chase, A.B., 1961. Pressure and temperature of crystallization from elastic effects around solid inclusions in minerals?. American Journal of Science, 259(7), pp.519-541.

Rovati, M., 2004. Directions of auxeticity for monoclinic crystals. Scripta materialia, 51(11), pp.1087-1091.

Rutter, E. H. 1983. Pressure solution in nature, theory and experiment. Journal of the Geological Society, 140(5), 725-740.

Ryzhova, T. V. 1964. Elastic properties of plagioclases, Akad. SSSR Izv. Ser. Geofiz., 7, 1049–1051.

Serra, A., & Bacon, D. J. (1996). A new model for {10 1 2} twin growth in hcp metals. Philosophical Magazine A, 73(2), 333-343.

Sinogeikin, S.V., Schilling, F.R. & Bass, J.D., 2000. Single crystal elasticity of lawsonite. American Mineralogist, 85(11-12), pp.1834-1837.

Tan, J.C., Civalleri, B., Erba, A. & Albanese, E., 2015. Quantum mechanical predictions to elucidate the anisotropic elastic properties of zeolitic imidazolate frameworks: ZIF-4 vs. ZIF-zni. CrystEngComm, 17(2), pp.375-382.

Tatham, D.J., Lloyd, G.E., Butler, R.W.H. & Casey, M., 2008. Amphibole and lower crustal seismic properties. Earth and Planetary Science Letters, 267(1-2), pp.118-128.

Thomas, L.A. & Wooster, W.A., 1951. Piezoerescence—the growth of Dauphiné twinning in quartz under stress. Proceedings of the Royal Society of London. Series A. Mathematical and Physical Sciences, 208(1092), pp.43-62.

Thyng, K.M., Greene, C.A., Hetland, R.D., Zimmerle, H.M. and DiMarco, S.F., 2016. True colors of oceanography: Guidelines for effective and accurate colormap selection. Oceanography, 29(3), pp.9-13.

Timms, N.E., Healy, D., Reyes□Montes, J.M., Collins, D.S., Prior, D.J. & Young, R.P., 2010. Effects of crystallographic anisotropy on fracture development and acoustic emission in quartz. Journal of Geophysical Research: Solid Earth, 115(B7).

Timms, N. E., Reddy, S. M., Healy, D., Nemchin, A. A., Grange, M. L., Pidgeon, R. T., & Hart, R. 2012. Resolution of impact□related microstructures in lunar zircon: A shock□deformation mechanism map. Meteoritics & Planetary Science, 47(1), 120-141.

Timms, N.E., Erickson, T.M., Pearce, M.A., Cavosie, A.J., Schmieder, M., Tohver, E., Reddy, S.M., Zanetti, M.R., Nemchin, A.A. & Wittmann, A., 2017. A pressure-temperature phase diagram for zircon at extreme conditions. Earth-Science Reviews, 165, pp.185-202.

Timms, N.E., Healy, D., Erickson, T.M., Nemchin, A.A., Pearce, M.A. & Cavosie, A.J. 2018. The role of elastic anisotropy in the development of deformation microstructures in zircon. In: Moser, D., Corfu, F., Reddy, S., Darling, J., Tait, K. (Eds.), AGU Monograph: Microstructural Geochronology; Lattice to Atom-Scale Records of Planetary Evolution. AGU-Wiley, 183-202.

Timms, N.E., Pearce, M.A., Erickson, T.M., Cavosie, A.J., Rae, A.S., Wheeler, J., Wittmann, A., Ferrière, L., Poelchau, M.H., Tomioka, N. & Collins, G.S., 2019. New shock microstructures in titanite (CaTiSiO 5) from the peak ring of the Chicxulub impact structure, Mexico. Contributions to Mineralogy and Petrology, 174(5), p.38.

Thompson, N., & Millard, D. J. 1952. XXXVIII. Twin formation, in cadmium. The London, Edinburgh, and Dublin Philosophical Magazine and Journal of Science, 43(339), 422-440.

Ting, T.C.T. & Chen, T., 2005. Poisson's ratio for anisotropic elastic materials can have no bounds. The quarterly journal of mechanics and applied mathematics, 58(1), pp.73-82.

Tommasi, A., Gibert, B., Seipold, U. & Mainprice, D., 2001. Anisotropy of thermal diffusivity in the upper mantle. Nature, 411(6839), p.783.

Tomé, C. N., & Lebensohn, R. A. 2009. Manual for Code Visco-Plastic Self-Consistent (VPSC) (Version 7c). Los Alamos National Laboratory, USA

Tullis, J., 1970. Quartz: preferred orientation in rocks produced by Dauphiné twinning. Science, 168(3937), pp.1342-1344.

Turley, J. & Sines, G., 1971. The anisotropy of Young's modulus, shear modulus and Poisson's ratio in cubic materials. Journal of Physics D: Applied Physics, 4(2), p.264.

Van der Molen, I. & Van Roermund, H.L.M., 1986. The pressure path of solid inclusions in minerals: the retention of coesite inclusions during uplift. Lithos, 19(3-4), pp.317-324.

Vavryčuk, V., 2005. Focal mechanisms in anisotropic media. Geophysical Journal International, 161(2), pp.334-346.

Verma, R.K., 1960. Elasticity of some high□density crystals. Journal of Geophysical Research, 65(2), pp.757-766.

Waeselmann, N., Brown, J.M., Angel, R.J., Ross, N., Zhao, J. & Kaminsky, W., 2016. The elastic tensor of monoclinic alkali feldspars. American Mineralogist, 101(5), pp.1228-1231.

Walker, A.M. & Wookey, J., 2012. MSAT—A new toolkit for the analysis of elastic and seismic anisotropy. Computers & Geosciences, 49, pp.81-90.

Weidner, D.J. & Carleton, H.R., 1977. Elasticity of coesite. Journal of Geophysical Research, 82(8), pp.1334-1346.

Wenk, H.R., Janssen, C., Kenkmann, T. & Dresen, G., 2011. Mechanical twinning in quartz: shock experiments, impact, pseudotachylites and fault breccias. Tectonophysics, 510(1-2), pp.69-79.

Wheeler, J. 1992. Importance of pressure solution and Coble creep in the deformation of polymineralic rocks. Journal of Geophysical Research: Solid Earth, 97(B4), 4579-4586.

Wheeler, J., 2018. The effects of stress on reactions in the Earth: Sometimes rather mean, usually normal, always important. Journal of Metamorphic Geology, *36*(4), pp.439-461.

Wu, Y., Yi, N., Huang, L., Zhang, T., Fang, S., Chang, H., Li, N., Oh, J., Lee, J.A., Kozlov, M. & Chipara, A.C., 2015. Three-dimensionally bonded spongy graphene material with super compressive elasticity and near-zero Poisson's ratio. Nature communications, 6, p.6141.

Yeganeh-Haeri, A., Weidner, D.J. & Parise, J.B., 1992. Elasticity of α-cristobalite: a silicon dioxide with a negative Poisson's ratio. Science, 257(5070), pp.650-652.

Zhang, Y., 1998. Mechanical and phase equilibria in inclusion–host systems. Earth and Planetary Science Letters, 157(3-4), pp.209-222.

Zhou, B. & Greenhalgh, S., 2004. On the computation of elastic wave group velocities for a general anisotropic medium. Journal of Geophysics and Engineering, 1(3), pp.205-215.